



HAL
open science

Structure and allosteric inhibition mechanism of excitatory amino acid transporter 1

Juan C Canul-Tec, Reda Assal, Erica Cirri, Pierre Legrand, Sébastien Brier,
Julia Chamot-Rooke, Nicolas Reyes

► **To cite this version:**

Juan C Canul-Tec, Reda Assal, Erica Cirri, Pierre Legrand, Sébastien Brier, et al.. Structure and allosteric inhibition mechanism of excitatory amino acid transporter 1. *Nature*, 2017, 544 (7651), pp.446 - 451. 10.1038/nature22064. hal-03053914v1

HAL Id: hal-03053914

<https://pasteur.hal.science/hal-03053914v1>

Submitted on 5 Dec 2017 (v1), last revised 11 Dec 2020 (v2)

HAL is a multi-disciplinary open access archive for the deposit and dissemination of scientific research documents, whether they are published or not. The documents may come from teaching and research institutions in France or abroad, or from public or private research centers.

L'archive ouverte pluridisciplinaire **HAL**, est destinée au dépôt et à la diffusion de documents scientifiques de niveau recherche, publiés ou non, émanant des établissements d'enseignement et de recherche français ou étrangers, des laboratoires publics ou privés.



Distributed under a Creative Commons Attribution - NonCommercial - ShareAlike 4.0 International License

1
2
3
4
5
6
7
8
9
10
11
12
13
14
15
16
17
18
19
20

Structure and allosteric inhibition mechanism of excitatory amino acid transporter 1

Juan C. Canul-Tec^{1,4#}, Reda Assal^{1,4#}, Erica Cirri^{1,4}, Pierre Legrand², Sébastien Brier^{3,4}, Julia Chamot-Rooke^{3,4} & Nicolas Reyes^{1,4*}

¹Molecular Mechanisms of Membrane Transport Laboratory, Institut Pasteur, 25–28 rue du Docteur Roux, 75015 Paris, France

²Synchrotron SOLEIL, L'Orme des Merisiers, 91192 Gif-sur-Yvette, France

³Structural Mass Spectrometry and Proteomics Unit, Institut Pasteur, 25–28 rue du Docteur Roux, 75015 Paris, France

⁴UMR 3528, CNRS, Institut Pasteur, 25–28 rue du Docteur Roux, 75015 Paris, France

[#]These authors contributed equally to this work

*Correspondence and requests for materials should be addressed to N.R. (nreyes@pasteur.fr)

21

22

23 **Abstract**

24 Human members of the solute carrier 1 (SLC1) family of transporters take up
25 excitatory neurotransmitters in the brain and amino acids in peripheral organs.

26 Dysregulation of their functions is associated to neurodegenerative disorders and

27 cancer. Here we present the first crystal structures of a thermostabilized human SLC1

28 transporter, the excitatory amino acid transporter 1 (EAAT1), with and without

29 allosteric and competitive inhibitors bound. The structures show novel architectural

30 features of the human transporters, including intra- and extracellular domains with

31 potential roles in transport function, as well as regulation by lipids and post-

32 translational modifications. The coordination of the inhibitor in the structures and the

33 change in the transporter dynamics measured by hydrogen-deuterium exchange mass

34 spectrometry, reveal an allosteric mechanism of inhibition, whereby the transporter is

35 locked in the outward-facing states of the transport cycle. Our results provide

36 unprecedented insights into the molecular mechanisms of function and pharmacology

37 of human SLC1 transporters.

38

39 SLC1 transporters constitute a large family of ion-coupled amino acid
40 transporters present in all kingdoms of life¹. In humans, there are seven SLC1
41 transporters that share 40-70% amino acid identity (Extended Data Fig. 1) and have
42 evolved to serve two specialized functions²: in the central nervous system, SLC1
43 excitatory amino acid transporters (EAAT1-5) take up the neurotransmitter glutamate
44 into the cell. In peripheral organs, EAATs take up glutamate and aspartate, while
45 neutral amino acid transporters (ASCT1-2) exchange small amino acids between the
46 extra- and intracellular compartments, contributing to the cellular solute homeostasis.

47 Glutamate is the most important excitatory transmitter in the mammalian brain
48 and is involved in most aspects of brain physiology, from development to cognition³.
49 Notably, most of the glutamate in the brain is intracellular, and it has to be
50 continuously pumped into the cytoplasm to allow for rounds of transmission and
51 prevent cytotoxicity. This essential neurological function is done by the EAAT1-5
52 isoforms expressed at the plasma membrane of astrocytes and neurons. In particular,
53 astroglial EAAT1 and EAAT2 orthologs are highly expressed in the hind- and
54 forebrain, respectively, and are responsible for most of the glutamate uptake in the
55 rodent brain⁴. EAATs are powerful molecular pumps capable of maintaining up to
56 10⁴-fold glutamate gradients by using energy stored in sodium, proton and potassium
57 gradients⁵. Remarkably, their dysregulation has been associated with several
58 neurological diseases, including amyotrophic lateral sclerosis⁶, ataxia^{7,8}, stroke⁹,
59 depression¹⁰ and glioma¹¹, making them important drug targets. Moreover, they are
60 also expressed in intestine and kidney, where mutations in EAAT3 have been
61 associated to dicarboxylic aminoaciduria¹².

62 ASCTs are structurally similar to EAATs, and function as sodium-dependent neutral
63 amino acid exchangers at the plasma membrane¹³. They are highly expressed in
64 intestine, kidney and testis, where they play a key role in maintaining the amino acid
65 cellular homeostasis. Importantly, ASCT2 is up-regulated in several forms of cancer,
66 including melanoma¹⁴, lung¹⁵, prostate¹⁶ and breast cancer¹⁷, and it is a key drug
67 target for the treatment and diagnosis of these diseases.

68 Despite the need for small compounds that selectively and allosterically
69 modulate SLC1 human transporters, most of their pharmacology is based on
70 substrate-analogs that inhibit transport with rather low selectivity among EAAT¹⁸ and
71 ASCT¹⁹ isoforms, respectively. Notably, the only known selective allosteric
72 modulators of SLC1 transporters are a series of non-competitive EAAT1-selective
73 inhibitors, of which 2-Amino-4-(4-methoxyphenyl)-7-(naphthalen-1-yl)-5-oxo-
74 5,6,7,8-tetrahydro-4H-chromene-3-carbonitrile (UCPH₁₀₁) is the best studied^{20,21}.
75 However, its mechanism of action is still poorly understood at the molecular level.

76 In structural terms, most our knowledge of the molecular mechanism of
77 transport and pharmacology of SLC1 transporters comes from the prokaryotic
78 homolog GltPh that has been crystallized in the main conformational states of the
79 transport cycle, outward-²² and inward-facing states^{23,24}, as well as in complex with a
80 non-selective and competitive inhibitor of the EAATs²⁵, DL-threo- β -
81 benzyloxyaspartic acid (TBOA). However, the presence of amino acid insertions and
82 deletions, as well as important differences in the transport function and pharmacology
83 of GltPh, make this homolog a limited structural model to understand the molecular
84 mechanism of the human SLC1 proteins.

85 Here we present 3.1-3.3 Å X-ray crystal structures of thermostable EAAT1
86 variants in complex with a substrate (L-aspartate), and the allosteric inhibitor

87 UCPH₁₀₁. The structures, and supporting functional data, show new architectural
88 features of the EAATs and ASCTs, and unravel the allosteric mechanism of
89 UCPH₁₀₁-like inhibitors in atomic detail. Taken together, these structural data can
90 prove useful for the design of novel allosteric compounds with improved selectivity
91 for both EAATs and ASCTs.

92 **EAAT1 engineering and crystallization**

93 Purified wild-type EAAT1 shows a poly-disperse size-exclusion
94 chromatogram in detergent solutions, and lacks transport activity upon reconstitution
95 in synthetic liposomes (Fig. 1a). To confer stability to EAAT1, we introduced
96 consensus mutations²⁶ in the predicted transmembrane helices, and obtained a
97 biochemically stable and functional transporter (Extended Data Fig. 1). As the protein
98 was still refractory to crystallization, we hypothesized that the extracellular region of
99 the transporter between the predicted transmembrane helix 3 (TM3) and the
100 cytoplasmic half of TM4 (TM4c) could preclude crystal growth due to the presence of
101 a long amino acid insertion compared to GltPh. We therefore engineered a chimeric
102 transporter substituting this region with the corresponding amino acid sequence from
103 ASCT2, which is the shortest in this region among human SLC1 transporters
104 (Extended Data Fig. 1). The resulting transporter, called EAAT1_{cryst}, shares an overall
105 ~75% sequence identity with wild type EAAT1, and up to ~90% identity at the C-
106 terminal core of the protein, where the transported substrate and coupled ions are
107 expected to bind^{25,27-31}. Importantly, purified EAAT1_{cryst} reconstituted in liposomes
108 showed robust glutamate uptake that depended on opposite gradients of sodium and
109 potassium ions across the bilayer (Fig. 1a and Extended Data Fig. 2a), and was
110 inhibited by the EAAT1-selective compound UCPH₁₀₁ in a concentration-dependent
111 fashion (IC₅₀ of 4.5±0.3 μM, Hill coefficient 0.92±0.07) (Fig. 1b). These data show

112 that the transport mechanism and pharmacological selectivity are conserved in
113 EAAT1_{cryst}.

114 Notably, EAAT1_{cryst} formed crystals in the presence of UCPH₁₀₁ that diffract
115 X-rays anisotropically and up to 3.25 Å resolution, and we solved its inhibitor-bound
116 structure by molecular replacement (see Methods and Extended Data Table 1). As
117 EAAT1_{cryst} was refractory to crystallization in the absence of UCPH₁₀₁, we reasoned
118 that mutations in the inhibitor-binding pocket could aid with the crystallization of the
119 transporter. A construct carrying M231I and F235I mutations (EAAT1_{cryst-II}; Extended
120 Data Fig. 1), crystallized both in the presence and absence of the inhibitor, and
121 diffracted X-rays up to 3.1 and 3.32 Å resolution, respectively (Extended Data Table
122 1). Remarkably, purified EAAT1_{cryst-II} reconstituted in liposomes also showed robust
123 sodium- and potassium-dependent glutamate uptake, while the UCPH₁₀₁ IC₅₀
124 increased >30-fold (>131±38 μM, Hill coefficient 0.92±0.0; Fig. 1a,b), as expected
125 for mutations in the binding pocket of the inhibitor (see below).

126 **Domain organization**

127 The structure of EAAT1_{cryst} shows a symmetric homotrimer in a substrate- and
128 UCPH₁₀₁-bound outward-facing conformation (Fig. 1c-e). EAAT1_{cryst} adopts an
129 overall GltPh-like fold^{22,23} (Extended Data Fig. 3), in which each monomer is
130 composed of two domains: a trimerization or scaffold domain (ScaD), including
131 TM1-2 and TM4-5; and a transport domain (TranD), including TM3, TM6-8 and re-
132 entrant helical loops 1-2 (HP1-2; Fig. 1f). The ScaD forms all inter-subunit contacts
133 through residues in TM2, TM4 and TM5, that include six salt bridges and bury
134 ~3,000 Å² from each subunit (Extended Data Fig. 4). Hence, the three ScaDs form a
135 compact central structure with a propeller-like shape that ensures the trimeric form of
136 the transporter and anchors it to the membrane.

137 The three TranDs are more peripheral and localize between the blades of the
138 propeller, making protein contacts exclusively with the ScaDs of their own monomer.
139 The TranD-ScaD interface buries $\sim 3,500 \text{ \AA}^2$, including a conserved salt bridge
140 between E256 and K364. This interface is mainly formed by cytoplasmic residues in
141 HP1, TM7, and TM3 (TranD), and TM2, TM4c, and TM5 (ScaD). However, on the
142 extracellular side additional contacts occurred between HP2 and TM4, through
143 residues that are well conserved among human transporters (Extended Data Fig. 5).

144 Substrate and ion translocation in SLC1 transporters is thought to occur
145 through large rigid-body movements of the TranD, relative to the static ScaD, that
146 move the cargo in an elevator-like fashion across the membrane^{23,32}. Thus, during the
147 isomerization to the inward-facing state the TranD-ScaD interface changes drastically
148 on the TranD side, and the novel features observed at this interface in EAAT1_{cryst}
149 might influence the distinct TranD dynamics in human SLC1 proteins.

150 **Transport domain**

151 One of the most remarkable architectural features of the EAAT1_{cryst} TranD is
152 at the TM8 level, in which deletions and insertions compared to GlTph reshape this
153 helix and its interactions with neighboring structural elements important for transport
154 (Fig. 2 and Extended Data Fig. 3). In EAAT1_{cryst}, TM8 can be divided into
155 extracellular (TM8a), transmembrane (TM8b), and cytoplasmic (TM8c) helices. The
156 loop connecting TM8a and the C-terminal helix of HP2 (HP2b) is six residues shorter
157 in human SLC1 transporters. Consequently, the extracellular ends of TM8a and HP2b
158 are in close proximity and engage in hydrogen bonding and hydrophobic interactions
159 (Fig. 2, upper right inset). HP2 is a key component of the gating machinery that
160 controls the access of substrate and ions to their binding sites in the TranD^{25,33-35}, and
161 its interactions with TM8b likely play an important role in determining HP2

162 movements. Notably, several single-cysteine mutations at positions along TM8a in
163 EAAT1³⁶, and in a rodent EAAT2 ortholog³⁷ impaired glutamate transport,
164 highlighting the significance of this extracellular region for function.

165 At TM8b level, we found strong electron density for the substrate (L-
166 aspartate) and one of the sodium-binding sites previously observed in the archeal
167 homologs of SLC1 family (Na2) (Fig. 2), which we modeled with similar
168 coordination than in their structures^{25,31}. Remarkably, the carboxylate group of D456
169 (TM8b), which coordinates the α -amino group of the substrate, is also at hydrogen
170 bond distance with the hydroxyl group of S343 (HP1). Moreover, the guanidinium
171 group of R457 (TM8b) engages in hydrogen bonding with HP1 residue G341, and
172 possibly L340 and T342 that point their backbone carbonyl oxygen atoms towards
173 TM8b. Residues S343 and R457 are well conserved in human SLC1 transporters, and
174 substitutions at equivalent positions in EAAT1 (S363 and R477)³⁸, and EAAT3
175 (R445)³⁹ inactivate transport. In addition, the loss-of-function mutation R445W in
176 EAAT3, equivalent to R457 in EAAT1_{crist}, causes human dicarboxylic aminoaciduria
177 due to the lack of aspartate/glutamate reabsorption function in the kidney¹². Overall,
178 the functional studies and our structural data converge to suggest that interactions
179 between conserved human residues at HP1 and TM8b are important to the correct
180 folding and function of the transporters.

181 On the cytoplasmic side, hydrophilic TM8c extends beyond the membrane
182 plane through a hydrophilic helix (TM8c), and makes contact with residues in TM3
183 and TM7a (Fig. 2, lower right inset). Notably, EAAT2 deletion mutants in this region
184 have a deleterious effect on transport function and membrane trafficking⁴⁰.
185 Accordingly, a deletion of TM8c beyond E501 in EAAT1 (equivalent to E500 in
186 EAAT2 and E481 in EAAT1_{crist}) decreased glutamate uptake rate by ~2-fold

187 (Extended Data Fig. 2b). The functional data, and the amino acid conservation in
188 TM8c among EAATs, underscore the pivotal role of this structural motif in protein
189 folding and transport kinetics.

190 **Scaffold domain**

191 The ScaD is less conserved than the TranD in the SLC1 family. In particular,
192 TM4 is highly divergent (Extended Data Fig. 1), and shows several unique
193 architectural features in EAAT1_{cryst}. On the extracellular side, TM4a forms inter- and
194 intra-monomeric contacts with TM2 and HP2, respectively. Moreover, an amino acid
195 insertion between TM4b and TM4c (TM4b-c loop) that appeared during the evolution
196 of eukaryotic transporters protrudes into the central vestibule of the EAAT1_{cryst} trimer
197 (Fig. 3a and Extended Data Fig. 4). The TM4b-c loop forms the center of the
198 propeller, and makes extensive contacts within and between protomers. Due to the
199 lack of electron density it was not possible to model the outermost residues of the
200 TM4b-c loop (Y200-V210), but they are expected to reach out to the bulk solvent,
201 and expose one of the predicted N-glycosylation sites of the transporter (N204).
202 Notably, despite the lack of sequence identity among human SLC1 transporters, all of
203 them contain predicted N-glycosylation sites in the TM4b-c loop, suggesting a
204 common role of this loop in the posttranslational processing of these proteins.

205 An additional novel feature of the EAAT1_{cryst} ScaD architecture is the N-
206 terminal extension of TM1 by an amphipathic helix (TM1a). Positioned nearly
207 parallel to the membrane plane, TM1a forms the tips of the blades in the propeller
208 (Fig. 1c and Fig. 3b). Remarkably, it does not form inter- or intra-monomeric
209 contacts, and its position and amphipathic nature suggest that TM1a somehow
210 interacts with the inner leaflet of the membrane. Indeed, there is a hydrophobic
211 crevice between TM1a and HP1a from the same monomer, where we observe strong

212 non-protein electron density in EAAT1_{cryst} that likely corresponds to bound detergent
213 or lipid molecules (Fig. 3b). Interestingly, a second hydrophobic crevice is observed
214 between the extracellular part of TM4 and HP2, where there is also strong non-protein
215 electron density (Fig. 3a). A similar crevice was also noted in a substrate-bound
216 structure of GltPh²².

217 The lipidic composition of the bilayer regulates the function of SLC1
218 transporters⁴¹⁻⁴⁵. Because TM1a-HP1a and TM4-HP2 hydrophobic crevices are at the
219 interface between the TranD and ScaD, where large conformational changes are
220 expected to occur during substrate translocation, they might constitute sites for lipid
221 regulation of transport function.

222 **UCPH₁₀₁ binding site**

223 The structure of EAAT1_{cryst} showed strong electron density for UCPH₁₀₁ in a
224 hydrophobic pocket facing the inner leaflet of the membrane on the interface between
225 the TranD and ScaD (Fig. 1d,e and Fig. 4a,b). This pocket is formed by residues in
226 TM3, TM7 and TM4c, and extends the TranD-ScaD interface by ~ 500 Å².

227 The chromene skeleton of UCPH₁₀₁, the parental group of the UCPH series of
228 compounds, is buried deeply in the domain interface, and coordinated by a direct ring-
229 stacking interaction with F369 (TM7a), as well as hydrophobic interactions with
230 G120 (TM3), V373 (TM7a) and M231 (TM4c) (Fig. 4b). In addition, the amine group
231 of UCPH₁₀₁ forms a hydrogen bond with the main-chain carbonyl of F369, while its
232 carbonitrile group interacts with Y127 (TM3). The methoxy-phenyl and naphthalene
233 groups are more peripheral and partly facing the hydrocarbon core of the membrane.
234 Yet, the former establishes hydrophobic interactions with V124 (TM3), V373 and
235 M231, while the latter is mainly coordinated by F235 (TM4c). The majority of the
236 above-mentioned residues have been reported to be important for the inhibition of an

237 EAAT1 rodent ortholog by UCPH₁₀₁ in cell assays²¹. Furthermore, the EAAT1_{cryst}
238 double mutant M231I-F235I (EAAT1_{cryst-II}) showed >30-fold increase in UCPH₁₀₁
239 IC₅₀ compared to EAAT1_{cryst} in proteo-liposomes (Fig. 1b). Hence, there is an
240 excellent agreement between the crystallographic and functional data.

241 Several mechanistically-relevant observations can be made regarding the
242 UCPH₁₀₁ binding pocket in EAAT1_{cryst}: i) it is over 15 Å away from the substrate and
243 sodium binding sites, suggesting that UCPH₁₀₁ does not preclude substrate binding, as
244 expected for a non-competitive allosteric inhibitor; ii) it faces the inner leaflet of the
245 membrane, implying that UCPH₁₀₁ accesses its binding site from the lipidic, and not
246 the aqueous phase, when applied extracellularly; iii) it is fully contained in a single
247 subunit, in agreement with the lack of cooperativity observed in proteo-liposome (Fig.
248 1b), and cell assays²¹; iv) a comparison of the EAAT1-5 sequences suggests that the
249 main determinants of UCPH₁₀₁ selectivity for EAAT1 are in TM4c, where M231 and
250 F235 are the only coordinating residues that differ between EAAT1 and all other
251 EAATs (Extended Data Fig. 1). Consistently, the equivalent residues in EAAT2 are
252 isoleucine, and the double mutant EAAT1_{cryst-II}, containing M231I and F235I, shows a
253 >30-fold increase in the UCPH₁₀₁ IC₅₀ compared to EAAT1_{cryst}.

254 **UCPH₁₀₁-unbound state**

255 To better understand the conformational changes of the transporter induced by
256 UCPH₁₀₁, we set out to determine the structure of the UCPH₁₀₁-unbound state. As
257 mentioned above, EAAT1_{cryst} was refractory to crystallization in the absence of the
258 compound and instead, we solved the structure of EAAT1_{cryst-II} UCPH₁₀₁-unbound
259 state. For comparison, we determined the structure of the EAAT1_{cryst-II} UCPH₁₀₁-
260 bound state, using a large excess of the compound in the crystallization conditions
261 (see Methods).

262 The structure of EAAT1_{cryst-II} in the UCPH₁₀₁-bound state is nearly identical to
263 that of the EAAT1_{cryst} with the exception of the mutated I231 and I235 side chains,
264 and a ~2 Å movement of UCPH₁₀₁ methoxy-phenyl and naphthalene groups away
265 from them (Fig. 4c and Extended Data Fig. 6a). Interestingly, the EAAT1_{cryst-II}
266 UCPH₁₀₁-unbound structure has an overall similar conformation to the UCPH₁₀₁-
267 bound state, but shows notable differences. First, the UCPH₁₀₁ binding pocket
268 contains no excess electron density, and the side chain of F369 moves outward by as
269 much as 1.9 Å, partly occupying the volume for UCPH₁₀₁ chromene group (Fig. 4c).
270 Second, there is a small rigid-body movement of the entire TranD that is shifted by as
271 much as 0.7 Å, compared to the UCPH₁₀₁-bound structures (Extended Data Fig. 6b).
272 Interestingly, this conformational change shows the EAAT1_{cryst} TranD is able to
273 undergo rigid-body movements relative to the ScaD, and highlights the importance of
274 such movements for the function of the human transporters, as it has been shown for
275 the prokaryotic homolog^{23,24}.

276 The structural changes observed in the UCPH₁₀₁-unbound structure
277 unambiguously demonstrate that the assigned binding pocket of UCPH₁₀₁ is correct,
278 and that within the restricted environment of the crystal lattice, UCPH₁₀₁ induces both
279 local and global conformational changes of the transporter that optimize its
280 coordination in an outward-facing state.

281 **Transport domain dynamics**

282 The coordination of UCPH₁₀₁ in the crystal structures, wedged between the
283 TranD (TM3 and TM7a) and the ScaD (TM4c), as well as the effect of the M231I-
284 F235I mutations on the UCPH₁₀₁ potency strongly suggest that UCPH₁₀₁ inhibits
285 transport by trapping the transporter in an outward-facing state. Consistently, the
286 rigid-body movements of the TranD to isomerize into the inward-facing state would

287 separate the coordinating residues in the TranD from those in the ScaD, and disrupt
288 the UCPH₁₀₁ coordination. Hence, under equilibrium conditions where the
289 transporters are sampling outward- and inward-facing states, the expected effect of
290 UCPH₁₀₁ binding is to shift the equilibrium in favor of the outward-facing state.

291 To gain insights into the effects of UCPH₁₀₁ binding to the transporters at
292 equilibrium, we probed the detergent solubilized EAAT1_{cryst} by hydrogen-deuterium
293 exchange mass spectrometry (HDX-MS). HDX-MS measures the rate of exchange of
294 backbone amide hydrogen atoms that depends on solvent accessibility and hydrogen
295 bonding, and provides valuable information on the dynamics and conformational
296 changes of proteins^{46,47}.

297 We compared the HDX behavior of the EAAT1_{cryst} in the presence and
298 absence of UCPH₁₀₁. Overall, the deuterium uptake pattern of EAAT1_{cryst} shows
299 dynamic structural elements in both the TranD and ScaD (Extended Data Fig. 7-9),
300 and reveals the unstructured and solvent-exposed nature of several regions that were
301 not resolved in the crystal structures, including the TM3-TM4a (peptide 153-173) and
302 TM4b-c (peptide 200-208) loops, as well as the N- (peptide 1-28) and C- termini
303 (peptides 490-522) (Extended Data Fig. 10).

304 Binding of UCPH₁₀₁ significantly decreased deuterium uptake in several areas
305 of the TranD including its binding pocket (residues 112-123 and 370-374), and the
306 surrounding area (residues 354-369), while it left the uptake in the ScaD unchanged
307 (Fig. 5a). It also decreased deuterium uptake in distant residues (336-349 and 420-
308 430) at the tips of HP1 and HP2 involved in substrate coordination and occlusion,
309 suggesting that UCPH₁₀₁ induces conformational changes in the transporter upon
310 binding. To gain insights into the nature of those conformational changes, we first
311 compared the TranD areas in which UCPH₁₀₁ decreased uptake with those buried at

312 the interface with ScaD in the EAAT1_{cryst} structure, and found that they correlate
313 remarkably well (Fig. 5a-c). Second, we built a model of the EAAT1_{cryst} inward-
314 facing state, based on a recently solved structure of GltPh²⁴, to assess the changes in
315 solvent accessibility in a possible transition between inward- and outward-facing
316 states (Fig. 5c,d). Indeed, the comparison between the structure and the model shows
317 that the UCPH₁₀₁-modified areas detected by HDX-MS transit as rigid bodies from
318 being solvent-exposed, in the inward-facing state, to buried at the TranD-ScaD
319 interface, in the outward-facing state. Such conformational change is expected to
320 decrease the dynamics of alpha helices and/or the solvent accessibility of the loops in
321 the UCPH₁₀₁-modified areas and thus, is consistent with the observed decrease in
322 deuterium uptake. Overall, the HDX-MS and structural analysis support the
323 stabilization of the outward-facing state, at the expense of the inward-facing state(s),
324 induced by UCPH₁₀₁.

325 **UCPH₁₀₁- and TBOA_{TFB}-bound state**

326 The distant position of UCPH₁₀₁ from the substrate and the HP2, a structural
327 element that controls extracellular access to the binding site²⁵, suggests that the
328 UCPH₁₀₁-bound transporters could undergo the conformational changes required to
329 exchange the substrate with the extracellular solution. To test this, we solved the
330 crystal structure of EAAT1_{cryst} in complex with both UCPH₁₀₁ and (2*S*,3*S*)-3-[3-[4-
331 (trifluoromethyl)benzoylamino]benzyloxy]aspartate (TBOA_{TFB}), a potent and non-
332 selective TBOA derivative⁴⁸, at 3.7 Å resolution (Extended Data Table 1).

333 Overall, the UCPH₁₀₁-TBOA_{TFB} bound structure is similar to that of the UCPH₁₀₁-
334 bound state, with the exception of HP2 that adopts an “open” conformation and packs
335 against the TM4b-c loop, disrupting the coordination of the Na₂ (Fig. 6a,b). These
336 conformational changes resemble those previously observed in the structure of the

337 GltPh-TBOA complex, and are in excellent agreement with the proposed competitive
338 inhibitory mechanism of TBOA-like compounds²⁵.

339 In the substrate-binding site, we observed excess electron density for the bulky
340 TBOA_{TFB} (Fig. 6c), but due to lack of resolution, we were not able to unambiguously
341 orient the compound. In order to fit the TBOA_{TFB} molecule into the density, we
342 initially positioned the TBOA moiety of TBOA_{TFB} using the TBOA-bound GltPh
343 structure as a guide. In this position, it remained stable during several successive
344 cycles of refinement that yielded a reasonable fit into the electron density. The
345 additional benzoylamino and trifluoromethyl groups of TBOA_{TFB} localized in a
346 hydrophobic cavity mainly formed by residues in HP1b and TM7a, and possibly by
347 residues in TM2 and TM4c. Interestingly, the interactions of these groups with the
348 transporter could explain the ~1500-fold increase in inhibitory potency of TBOA_{TFB},
349 compared to TBOA, that has been observed in EAAT1 transport assays⁴⁸.

350 Indeed, we also observed UCPH₁₀₁ bound in this structure with an identical
351 coordination than in the substrate-bound state. Therefore, despite the lower resolution
352 of the TBOA_{TFB} bound structure, it shows that UCPH₁₀₁ binding at its allosteric site
353 does not preclude the movements of HP2 involved in substrate and sodium binding
354 from the extracellular solution.

355 **Inhibitory mechanisms of EAAT1**

356 The structures of EAAT1_{cyst} reveal new architectural features of human SLC1
357 transporters, and the first non-competitive inhibitory mechanism of this family of
358 proteins in molecular detail. UCPH₁₀₁ is an EAAT1-selective inhibitor with a bipartite
359 coordination by residues in both the TranD and ScaD, and the downward rigid-body
360 movements of the TranD during transport disrupt such coordination. This implies that
361 upon binding, UCPH₁₀₁ “glues” the TranD to the ScaD in the outward-facing states,

362 and precludes the translocation reaction of the transport cycle, but not the substrate
363 binding/unbinding reactions from the extracellular solution (Fig. 7).

364 The inhibitory mechanism of UCPH₁₀₁ contrasts with that of substrate-analog
365 competitive inhibitors like TBOA. The binding pocket of TBOA-like compounds
366 overlap to some extent with that of the substrate²⁵, and some of these molecules can
367 bind the transporter from both the extra- and intracellular aqueous solutions^{49,50}.
368 Therefore, they inhibit transport by precluding substrate binding on either side of the
369 membrane. Moreover, TBOA-like compounds are not selective among glutamate
370 transporters due to the high amino acid conservation in the substrate-binding sites.

371 The mechanistic differences observed in UCPH₁₀₁ over other known inhibitors
372 make it an extremely valuable pharmacological tool, to isolate and study the
373 conformational changes that EAAT1 undergoes upon substrate and ion binding.
374 Remarkably, the UCPH₁₀₁ allosteric binding site observed in EAAT1_{cryst} highlights a
375 cavity that can facilitate the design of selective compounds for other human SLC1
376 transporters, and possibly the long-sought positive modulators of glutamate uptake.

377

378

379 **METHODS**

380 **Construct optimization**

381 We used fluorescence-detection size-exclusion chromatography (FSEC)⁵¹ to
382 screen solubilization conditions and EAAT1 variants fused to enhanced green
383 fluorescent protein (eGFP). EAAT1 N-terminal fusions solubilized in dodecanoyl
384 sucrose (DDS, Anatrace) were found to have good solubility and mono-dispersity by
385 FSEC in clear lysates. However, EAAT1 loses its transport activity and
386 chromatographic monodispersity upon purification. To increase its stability, we used
387 consensus mutagenesis²⁶, and screened EAAT1 variants with different consensus
388 mutations in the predicted transmembrane helices by FSEC. The apparent melting
389 temperature (T_m) of the most stable EAAT1 construct was >20 °C over that of the
390 wild-type EAAT1, but the mutated transporter was still refractory to crystallization.
391 We reasoned that the extracellular region between TM3-4c could interfere with
392 crystallization, and changed it for the shorter TM3-4c sequence from ASCT2
393 (Extended Data Fig.1). In addition, we mutated the two predicted N-glycosylation
394 sites of the transporter (N155T and N204T mutations) to further improve
395 crystallizability.

396 **Expression and purification**

397 All constructs were introduced into pcDNA3.1(+) (Invitrogen) with N-
398 terminal Strep-tag II affinity tag followed by eGFP and PreScission protease cleavage
399 site, and expressed in HEK293F cells (ATCC, mycoplasma test negative) grown in
400 Excell293 medium (Sigma) and supplemented with 4mM L-glutamine (Sigma) and
401 5µg/ml Phenol red (Sigma-Aldrich) to densities of 2.5 x 10⁶ cells ml⁻¹. Cells were
402 transiently transfected in Freestyle293 medium (Invitrogen) using poly-ethylenimine
403 (PEI) (Tebu-bio) at a density of 2.5 x 10⁶ cells ml⁻¹, diluted with an equivalent volume

404 of Excell293 6 hours post-transfection, and treated with 2.2 mM valproic acid
405 (Sigma) 12 hours after dilution of the cultures. Cells were collected at ~48 h post-
406 transfection.

407 Initial screens of constructs and detergent solubilization buffers were done in
408 small-scale (5-10 ml), and cells were collected, mechanically disrupted with a
409 douncer and solubilized in 50 mM HEPES/Tris-base, pH 7.4, 200 mM NaCl buffer
410 supplemented with 1 mM L-asp, 1 mM EDTA, 1 mM Phenylmethylsulfonyl fluoride
411 (PMSF), 1 mM Tris(2-carboxyethyl)phosphine (TCEP), 1:200 (v/v) dilution of
412 mammalian protease inhibitor cocktail (Sigma), 10 % glycerol, 2% detergent and
413 0.4% cholesterol hemisuccinate (CHS) (Anatrace). After 1-hour incubation at 4 °C,
414 clear lysates were obtained by ultracentrifugation (247,000 g for 45 min). A high-
415 throughput auto-sampler was used to inject the lysates in a SRT SEC-500 column
416 (Sepax Technologies) equilibrated in 50 mM HEPES/Tris-base, pH 7.4, 200 mM
417 NaCl buffer supplemented with 1 mM L-asp, 1 mM (TCEP), 5 % glycerol, 3 x CMC
418 detergent, and ~0.01% CHS, in line with fluorescence detection (Photon technology
419 international) for FSEC analysis.

420 Large-scale expression was done in 2-4 l cultures with cells collected in 50
421 mM HEPES/Tris-base, pH 7.4, 50 mM NaCl buffer supplemented with 1 mM L-asp,
422 1 mM EDTA, 1 mM PMSF, 1 mM TCEP, and 1:200 (v/v) dilution of mammalian
423 protease inhibitor cocktail (Sigma), and disrupted in an cell homogenizer
424 (EmulsiFlex-C5, Avestin) after 3 runs at 15,000 Psi. The resulting homogenate was
425 clarified by centrifugation (4,500 g, 0.5 h) and the crude membranes were collected
426 by ultracentrifugation (186,000 g for 1.5 h). Membranes were washed once with the
427 above-mentioned buffer and finally homogenized with a douncer in a buffer
428 containing 50 mM HEPES/Tris-base, pH 7.4, 200 mM NaCl, 1 mM L-asp, 1 mM

429 EDTA, 1 mM TCEP, and 10% Glycerol, snap-frozen in liquid N₂ and stored at -80°C
430 at 0.5 g of membranes ml⁻¹.

431 Membrane solubilization was done by thawing out and supplementing the
432 membrane homogenate with 2% DDS, 0.4% CHS, and 25 μM UCPH₁₀₁ (Abcam).
433 After 1-hour incubation, the insoluble material was removed by ultracentrifugation
434 (186,000g for 1 h), and Strep-Tactin sepharose resin (GE Healthcare) was added to
435 the supernatant and rotated for 2 h. Resin was washed with 25 column volumes of 50
436 mM HEPES/Tris-base, pH 7.4, 200 mM NaCl, 1 mM L-asp, 1 mM TCEP, 5%
437 Glycerol, 0.05% DDS, 0.01% CHS and 25 μM UCPH₁₀₁, and the protein was eluted
438 with the same buffer supplemented with 2.5 mM D-desthiobiotin.

439 The eluted eGFP-transporter fusion was concentrated to 1-2 mg ml⁻¹ using
440 100-kDa cutoff membranes (Millipore), and digested with His-tagged PreScission
441 protease overnight at 4 °C. The protease was removed by reverse Ni-NTA (Qiagen)
442 affinity chromatography, and the flow through containing the transporter was
443 concentrated to 500 μl, ultra-centrifuged (86,900 g, 20 min), and applied to a
444 Superose 6 10/300 gel filtration column (GE Healthcare) equilibrated with 50 mM
445 HEPES/Tris-base, pH 7.4, 200 mM NaCl, 1 mM L-asp, 1 mM TCEP, 5% Glycerol,
446 0.25% decanoyl sucrose (DS, Sigma), 0.05% CHS and 100 μM UCPH₁₀₁. To obtain
447 the UCPH₁₀₁ unbound structure, the protocol was identical, but the allosteric inhibitor
448 was omitted from all buffers. To obtain the UCPH₁₀₁-TBOA_{TFB} bound structure, the
449 protein sample was supplemented with 3 mM TBOA_{TFB} (Tocris) before the injection
450 in the gel filtration column equilibrated with 50 mM HEPES/Tris-base, pH 7.4, 200
451 mM NaCl, 1 mM TCEP, 5% Glycerol, 0.25% decanoyl sucrose (DS, Sigma), 0.05%
452 CHS, 300 μM TBOA_{TFB} and 100 μM UCPH₁₀₁.

453 Protein samples after the solubilization step were kept on ice or at 4 °C at all times.

454 **Crystallization and structure determination**

455 Purified protein was concentrated to 3.5-4.0 mg ml⁻¹ and 1 mM UCPH₁₀₁ was
456 added in experiments with the inhibitor-bound transporters. Initial vapor diffusion
457 crystallization screens were done by mixing 300 nl of protein and reservoir solution in
458 sitting drops, dispensed by a Mosquito robot (TTP labtech) in 96-well Greiner plates.
459 The purified transporters form three-dimensional crystals in several conditions
460 containing low molecular weight polyethylene glycols. The best-diffracting crystals
461 were obtained after manual optimization using 1.6 µl hanging drops at 4 °C, obtained
462 by mixing equal volumes of protein supplemented with 0.2% n-Octyl-b-D-
463 glucopyranoside (BOG, Anatrace) and 0.04% CHS, and reservoir solutions containing
464 100 mM Tris, pH 8.2, 50 mM CaCl₂, 50 mM BaCl₂, and 28-30% PEG 400. Crystals
465 appeared after 24-48 h and reached their maximum size after a week. Crystals were
466 flash-frozen in liquid nitrogen before X-ray diffraction data collection without any
467 further cryo protection.

468 X-ray diffraction data were collected at beamlines PROXIMA-1 at the
469 SOLEIL synchrotron (St Aubin, France) and at beamlines at the European
470 Synchrotron Radiation Facility (Grenoble, France). In general, 2-3 data sets from
471 single crystals were collected, and indexed, integrated, scaled and merged using XDS
472 package⁵². Due to the anisotropic nature of the diffraction data, the DEBYE and
473 STARANISO programs were applied to scale it using the STARANISO server
474 (<http://staraniso.globalphasing.org/>). The software performs an anisotropic cut-off of
475 merged intensity data with a Bayesian estimation of the structure amplitudes, and
476 applies an anisotropic correction to the data. Table 1 shows the refinement statistics
477 for the full sets of reflections truncated at the best high-resolution along h, k or l axis,
478 values given by AIMLESS⁵³, before the anisotropic corrections computed by the

479 STARANISO software. The corrected anisotropic amplitudes were then used for
480 molecular replacement in PHASER⁵⁴, using the scaffold and transport domains of
481 GltPh (PDB code 2NWL) as independent search models. The initial electron density
482 maps were clearly interpretable, and the final model was obtained through rounds of
483 manual building in COOT⁵⁵ and refinement in Buster⁵⁶, until reaching good
484 crystallographic statistics and stereochemistry (Extended Data Table 1). The model
485 contains one EAAT1_{cryst} monomer per asymmetric unit and most of the EAAT1_{cryst}
486 polypeptide (residues 37-487), with the exception of some residues in the
487 extracellular loops between TM3-4a, TM4b-4c, TM5-6 and TM7b-HP2a. Sequence
488 assignment was aided by anomalous difference Fourier maps from diffraction data
489 collected with low energy X-rays (1.77 Å) to highlight the sulfur atoms of methionine
490 and cysteine residues (Extended Data Fig. 11). EAAT1_{cryst-II}, as well as the
491 EAAT1_{cryst} UCPH₁₀₁-TBOA_{TFB} bound structures were solved by the same approach
492 above mentioned, but using the EAAT1_{cryst} TranD and ScaD as independent search
493 models for molecular replacement.

494 The stereochemical properties of the final models were analyzed with the Molprobit
495 server (<http://molprobit.biochem.duke.edu/>). At least 95% of the residues in all
496 models are in the Ramachandran favored region. Protein interfaces were analyzed
497 with the PISA server (http://www.ebi.ac.uk/msd-srv/prot_int/pistart.html). Structural
498 alignments were done with Superpose in the CCP4 suite. All structural figures were
499 prepared with PyMOL Molecular Graphics System, Schrodinger, LLC.

500 **Radioactive substrate transport assays**

501 Unilamellar liposomes were made at 9:1 molar ratio of 1-palmitoyl-2-oleoyl-
502 sn-glycero-3-phosphocholine (Avanti Polar Lipids) and CHS, in a buffer containing
503 50 mM HEPES/Tris-base, pH 7.4, 200 mM NaCl and 1 mM L-asp. The transporters

504 were purified as described above, but excluding the reverse chromatography step after
505 protease cleavage, and using a Superose 6 10/300 column equilibrated with 50 mM
506 HEPES/Tris-base, pH 7.4, 200 mM NaCl, 1 mM L-asp, 0.5 mM TCEP, 0.0632%
507 DDS, 0.01264% CHS, and 5% glycerol.

508 To reconstitute the protein, liposomes were first mixed with DDS at a 1:2
509 (w/w) lipid-to-detergent ratio for 1 h, and then the purified transporters were added at
510 a 1:40 (w/w) protein-to-lipid ratio. Detergent removal was done at 4° C using SM-2
511 biobeads (BioRad) at 100 mg ml⁻¹. The internal solution of the liposomes was
512 exchanged using 10 freeze-thaw cycles in the appropriate buffer. After extrusion
513 through 400-nm polycarbonate membranes (Avanti Polar Lipids), the
514 proteoliposomes were concentrated by ultracentrifugation (150,000 g for 30 min at
515 4°C) and resuspended at 20 mg of lipids ml⁻¹, for immediate use.

516 Substrate transport was assayed at 37°C. The uptake reaction was initiated by
517 diluting the proteo-liposomes 10-fold into a buffer containing 50 mM HEPES/Tris-
518 base, pH 7.4, 200 mM NaCl, 50 µM L-glutamate, and 5 µM [¹⁴C]-L-glutamate
519 (PerkinElmer), and 2.5% glycerol. After 30 min, 200-µl aliquots were diluted 5-fold
520 into ice-cold quench buffer (50 mM HEPES/Tris-base, pH 7.4, 200 mM ChCl, and
521 2.5% glycerol), followed by immediate filtration and wash on nitrocellulose 0.22-µm
522 filters (Millipore). Radioactivity was quantified by liquid scintillation using a Tri-
523 Carb 3110TR counter (PerkinElmer). For the UCPH₁₀₁ titrations, proteo-liposomes
524 were both pre-incubated for 20 min at room temperature, and assayed in the presence
525 of UCPH₁₀₁. Background radioactivity was estimated from protein-free liposomes,
526 and subtracted from the uptake data. Data was fitted to a Hill equation of the form:

527
$$F = F_{\infty} + \Delta F_{\infty} / (1 + (IC_{50} / [UCPH_{101}])^n)$$

528 Where F_{∞} is the final level of inhibition, ΔF_{∞} is the final amplitude of the UCPH₁₀₁
529 effect, and n is the Hill coefficient.

530 To titrate the rate of L-glutamate transport by EAAT1_{cryst}, proteo-liposomes were
531 assayed in the presence of 0, 5, 50 or 200 μ M L-glutamate supplemented with 1, 5, 5,
532 or 5 μ M [¹⁴C]-L-glutamate, respectively. At each substrate concentration, the initial
533 rate of transport was calculated by a linear fit to 120 s and 180 s uptake measurements
534 with origin fixed at zero. Background radioactivity was estimated from protein-free
535 liposomes, and subtracted from the uptake data.

536 For the cell-based transport uptake, cells were collected 36 h post-transfection, and
537 washed three times and resuspended at a density of 50×10^6 cells ml⁻¹ in 11 mM
538 HEPES/Tris-base, pH 7.4, 140 mM ChCl, 4.7 mM KCl, 2.5 mM CaCl₂, 1.2 mM
539 MgCl₂, and 10 mM D-glucose, for immediate use. The uptake assay was performed
540 similarly to the one described for the proteo-liposomes, but using a reaction buffer
541 containing 11 mM HEPES/Tris-base, pH 7.4, 140 mM NaCl, 4.7 mM KCl, 2.5 mM
542 CaCl₂, 1.2 mM MgCl₂, 10 mM D-glucose, 50 μ M L-glutamate, and 5 μ M [¹⁴C]-L-
543 glutamate, and 0.8- μ m nitrocellulose filters. Background radioactivity was estimated
544 from cells transfected with empty vector, and subtracted from the uptake data.

545 **Hydrogen-deuterium exchange mass spectrometry**

546 HDX-MS experiments were performed with transporters purified as described
547 in the proteo-liposome section, and using a Superose 6 5/150 gel filtration column
548 equilibrated with 50 mM HEPES/Tris-base, 200 mM NaCl, pH7.4, 1 mM L-asp, 0.5
549 mM TCEP, 0.0632% DDS, 0.01264% CHS, and 5% glycerol.

550 The purified EAAT1_{cryst} was incubated in ice for 30 min with 2.2% DMSO at
551 a monomer concentration of 5.2 μ M, in the presence and absence of 102 μ M
552 UCPH₁₀₁, respectively. Prior to labeling, 10 μ L of the unbound and UCPH₁₀₁-bound

553 EAAT1_{cryst} solution was equilibrated for 10 min at room temperature. Deuterium
554 exchange was initiated by adding 40 μ L of D₂O buffer (50 mM HEPES, pD 7.3, 200
555 mM NaCl, 1 mM L-asp, 5% glycerol, 0.0632% DDS, 0.01264% CHS, 0.5 mM
556 TCEP) supplemented or not with 101.2 μ M UCPH₁₀₁. Assuming that the K_D and IC_{50}
557 values of UCPH₁₀₁ are similar, ~96% of the transporters would remain bound during
558 deuterium labeling. Aliquots of 10.4 pmols of protein were removed at defined
559 deuterium exchange time points (from 10 sec to 60 min) and quenched upon mixing
560 with an ice-cold acidic solution (0.75% formic acid, 5% glycerol) to decrease the pH
561 to 2.6. Quenched samples were immediately snap-frozen in liquid N₂ and stored at -
562 80°C until analysis.

563 Prior to mass analysis, quenched samples were rapidly thawed and
564 immediately injected into a cooled nanoACQUITY UPLC HDX system (Waters
565 corp.) maintained at 0°C. 8.6-pmol protein samples were on-line digested for 2 min at
566 20 °C using an in-house packed immobilized pepsin cartridge (2.0 x 20 mm, 66 μ L
567 bed volume). The resulting peptides were trapped and desalted onto a C18 Trap
568 column (VanGuard BEH 1.7 μ m, 2.1 x 5 mm, Waters corp.) at a flow rate of 100
569 μ L/min of 0.15% formic acid, and then separated in 10 min by a linear gradient of
570 acetonitrile from 5 to 40% at 40 μ L/min using an ACQUITY UPLCTM BEH C18
571 analytical column (1.7 μ m, 1 x 100 mm, Waters corp.). After each run, the pepsin
572 cartridge was manually cleaned with two consecutive washes of 1% formic acid, 5%
573 acetonitrile, 1.5 M guanidinium chloride, pH 2.5. Blank injections were performed
574 between each run to confirm the absence of carry-over.

575 Mass spectra were acquired in resolution and positive mode on a Synapt G2-Si
576 HDMS mass spectrometer (Waters corp.) equipped with a standard electrospray
577 ionization source, as described previously⁵⁷. Peptides were identified from

578 undeuterated protein samples acquired in MS^E mode by database searching in
579 ProteinLynX Global Server 3.0 (Waters corp.). Each fragmentation spectrum was
580 manually inspected for assignment validation. Deuterium uptake values were
581 calculated for each peptide using DynamX 3.0 (Waters corp.). Only one unique
582 charge state was considered per peptide and no adjustment was made for back-
583 exchange. HDX-MS results are reported as relative deuterium uptake values
584 expressed in mass unit or fractional exchange⁵⁷. A statistical analysis was performed
585 with MEMHDX⁵⁸ using a False Discovery Rate of 1%.
586

587 **References**

- 588 1 Slotboom, D. J., Konings, W. N. & Lolkema, J. S. Structural features of the
589 glutamate transporter family. *Microbiol Mol Biol Rev* **63**, 293-307 (1999).
- 590 2 Kanai, Y. & Hediger, M. A. The glutamate and neutral amino acid
591 transporter family: physiological and pharmacological implications. *Eur J*
592 *Pharmacol* **479**, 237-247 (2003).
- 593 3 Danbolt, N. C. Glutamate uptake. *Prog Neurobiol* **65**, 1-105 (2001).
- 594 4 Lehre, K. P. & Danbolt, N. C. The number of glutamate transporter subtype
595 molecules at glutamatergic synapses: chemical and stereological
596 quantification in young adult rat brain. *J Neurosci* **18**, 8751-8757 (1998).
- 597 5 Zerangue, N. & Kavanaugh, M. P. Flux coupling in a neuronal glutamate
598 transporter. *Nature* **383**, 634-637, doi:10.1038/383634a0 (1996).
- 599 6 Rothstein, J. D., Van Kammen, M., Levey, A. I., Martin, L. J. & Kuncl, R. W.
600 Selective loss of glial glutamate transporter GLT-1 in amyotrophic lateral
601 sclerosis. *Ann Neurol* **38**, 73-84, doi:10.1002/ana.410380114 (1995).
- 602 7 Winter, N., Kovermann, P. & Fahlke, C. A point mutation associated with
603 episodic ataxia 6 increases glutamate transporter anion currents. *Brain*
604 **135**, 3416-3425, doi:10.1093/brain/aws255 (2012).
- 605 8 Choi, K. D. *et al.* Late-onset episodic ataxia associated with SLC1A3
606 mutation. *J Hum Genet*, doi:10.1038/jhg.2016.137 (2016).
- 607 9 Chao, X. D., Fei, F. & Fei, Z. The role of excitatory amino acid transporters
608 in cerebral ischemia. *Neurochem Res* **35**, 1224-1230,
609 doi:10.1007/s11064-010-0178-3 (2010).
- 610 10 Pilc, A., Wieronska, J. M. & Skolnick, P. Glutamate-based antidepressants:
611 preclinical psychopharmacology. *Biol Psychiatry* **73**, 1125-1132,
612 doi:10.1016/j.biopsych.2013.01.021 (2013).
- 613 11 Robert, S. M. & Sontheimer, H. Glutamate transporters in the biology of
614 malignant gliomas. *Cell Mol Life Sci* **71**, 1839-1854, doi:10.1007/s00018-
615 013-1521-z (2014).
- 616 12 Bailey, C. G. *et al.* Loss-of-function mutations in the glutamate transporter
617 SLC1A1 cause human dicarboxylic aminoaciduria. *J Clin Invest* **121**, 446-
618 453, doi:10.1172/JCI44474 (2011).
- 619 13 Zerangue, N. & Kavanaugh, M. P. ASCT-1 is a neutral amino acid exchanger
620 with chloride channel activity. *J Biol Chem* **271**, 27991-27994 (1996).
- 621 14 Wang, Q. *et al.* Targeting glutamine transport to suppress melanoma cell
622 growth. *Int J Cancer* **135**, 1060-1071, doi:10.1002/ijc.28749 (2014).
- 623 15 Shimizu, K. *et al.* ASC amino-acid transporter 2 (ASCT2) as a novel
624 prognostic marker in non-small cell lung cancer. *Br J Cancer* **110**, 2030-
625 2039, doi:10.1038/bjc.2014.88 (2014).
- 626 16 Wang, Q. *et al.* Targeting ASCT2-mediated glutamine uptake blocks
627 prostate cancer growth and tumour development. *J Pathol* **236**, 278-289,
628 doi:10.1002/path.4518 (2015).
- 629 17 van Geldermalsen, M. *et al.* ASCT2/SLC1A5 controls glutamine uptake and
630 tumour growth in triple-negative basal-like breast cancer. *Oncogene* **35**,
631 3201-3208, doi:10.1038/onc.2015.381 (2016).
- 632 18 Shimamoto, K. Glutamate transporter blockers for elucidation of the
633 function of excitatory neurotransmission systems. *Chem Rec* **8**, 182-199,
634 doi:10.1002/tcr.20145 (2008).

- 635 19 Grewer, C. & Grabsch, E. New inhibitors for the neutral amino acid
636 transporter ASCT2 reveal its Na⁺-dependent anion leak. *J Physiol* **557**,
637 747-759, doi:10.1113/jphysiol.2004.062521 (2004).
- 638 20 Jensen, A. A. *et al.* Discovery of the first selective inhibitor of excitatory
639 amino acid transporter subtype 1. *J Med Chem* **52**, 912-915,
640 doi:10.1021/jm8013458 (2009).
- 641 21 Abrahamsen, B. *et al.* Allosteric modulation of an excitatory amino acid
642 transporter: the subtype-selective inhibitor UCPH-101 exerts sustained
643 inhibition of EAAT1 through an intramonomeric site in the trimerization
644 domain. *J Neurosci* **33**, 1068-1087, doi:10.1523/JNEUROSCI.3396-
645 12.2013 (2013).
- 646 22 Yernool, D., Boudker, O., Jin, Y. & Gouaux, E. Structure of a glutamate
647 transporter homologue from *Pyrococcus horikoshii*. *Nature* **431**, 811-818,
648 doi:10.1038/nature03018 (2004).
- 649 23 Reyes, N., Ginter, C. & Boudker, O. Transport mechanism of a bacterial
650 homologue of glutamate transporters. *Nature* **462**, 880-885,
651 doi:10.1038/nature08616 (2009).
- 652 24 Akyuz, N. *et al.* Transport domain unlocking sets the uptake rate of an
653 aspartate transporter. *Nature* **518**, 68-73, doi:10.1038/nature14158
654 (2015).
- 655 25 Boudker, O., Ryan, R. M., Yernool, D., Shimamoto, K. & Gouaux, E. Coupling
656 substrate and ion binding to extracellular gate of a sodium-dependent
657 aspartate transporter. *Nature* **445**, 387-393, doi:10.1038/nature05455
658 (2007).
- 659 26 Steipe, B., Schiller, B., Pluckthun, A. & Steinbacher, S. Sequence statistics
660 reliably predict stabilizing mutations in a protein domain. *J Mol Biol* **240**,
661 188-192, doi:10.1006/jmbi.1994.1434 (1994).
- 662 27 Zhang, Y., Bendahan, A., Zarbiv, R., Kavanaugh, M. P. & Kanner, B. I.
663 Molecular determinant of ion selectivity of a (Na⁺ + K⁺)-coupled rat brain
664 glutamate transporter. *Proc Natl Acad Sci U S A* **95**, 751-755 (1998).
- 665 28 Seal, R. P. & Amara, S. G. A reentrant loop domain in the glutamate carrier
666 EAAT1 participates in substrate binding and translocation. *Neuron* **21**,
667 1487-1498 (1998).
- 668 29 Tao, Z. *et al.* Mechanism of cation binding to the glutamate transporter
669 EAAC1 probed with mutation of the conserved amino acid residue
670 Thr101. *J Biol Chem* **285**, 17725-17733, doi:10.1074/jbc.M110.121798
671 (2010).
- 672 30 Larsson, H. P. *et al.* Evidence for a third sodium-binding site in glutamate
673 transporters suggests an ion/substrate coupling model. *Proc Natl Acad Sci*
674 *U S A* **107**, 13912-13917, doi:10.1073/pnas.1006289107 (2010).
- 675 31 Guskov, A., Jensen, S., Faustino, I., Marrink, S. J. & Slotboom, D. J. Coupled
676 binding mechanism of three sodium ions and aspartate in the glutamate
677 transporter homologue GltTk. *Nat Commun* **7**, 13420,
678 doi:10.1038/ncomms13420 (2016).
- 679 32 Crisman, T. J., Qu, S., Kanner, B. I. & Forrest, L. R. Inward-facing
680 conformation of glutamate transporters as revealed by their inverted-
681 topology structural repeats. *Proc Natl Acad Sci U S A* **106**, 20752-20757,
682 doi:10.1073/pnas.0908570106 (2009).

- 683 33 Focke, P. J., Moenne-Loccoz, P. & Larsson, H. P. Opposite movement of the
684 external gate of a glutamate transporter homolog upon binding
685 cotransported sodium compared with substrate. *J Neurosci* **31**, 6255-
686 6262, doi:10.1523/JNEUROSCI.6096-10.2011 (2011).
- 687 34 Brocke, L., Bendahan, A., Grunewald, M. & Kanner, B. I. Proximity of two
688 oppositely oriented reentrant loops in the glutamate transporter GLT-1
689 identified by paired cysteine mutagenesis. *J Biol Chem* **277**, 3985-3992,
690 doi:10.1074/jbc.M107735200 (2002).
- 691 35 Qu, S. & Kanner, B. I. Substrates and non-transportable analogues induce
692 structural rearrangements at the extracellular entrance of the glial
693 glutamate transporter GLT-1/EAAT2. *J Biol Chem* **283**, 26391-26400,
694 doi:10.1074/jbc.M802401200 (2008).
- 695 36 Seal, R. P., Leighton, B. H. & Amara, S. G. A model for the topology of
696 excitatory amino acid transporters determined by the extracellular
697 accessibility of substituted cysteines. *Neuron* **25**, 695-706 (2000).
- 698 37 Grunewald, M., Bendahan, A. & Kanner, B. I. Biotinylation of single
699 cysteine mutants of the glutamate transporter GLT-1 from rat brain
700 reveals its unusual topology. *Neuron* **21**, 623-632 (1998).
- 701 38 Ryan, R. M., Kortt, N. C., Sirivanta, T. & Vandenberg, R. J. The position of an
702 arginine residue influences substrate affinity and K⁺ coupling in the
703 human glutamate transporter, EAAT1. *J Neurochem* **114**, 565-575,
704 doi:10.1111/j.1471-4159.2010.06796.x (2010).
- 705 39 Borre, L. & Kanner, B. I. Arginine 445 controls the coupling between
706 glutamate and cations in the neuronal transporter EAAC-1. *J Biol Chem*
707 **279**, 2513-2519, doi:10.1074/jbc.M311446200 (2004).
- 708 40 Leinenweber, A., Machtens, J. P., Begemann, B. & Fahlke, C. Regulation of
709 glial glutamate transporters by C-terminal domains. *J Biol Chem* **286**,
710 1927-1937, doi:10.1074/jbc.M110.153486 (2011).
- 711 41 Shouffani, A. & Kanner, B. I. Cholesterol is required for the reconstruction
712 of the sodium- and chloride-coupled, gamma-aminobutyric acid
713 transporter from rat brain. *J Biol Chem* **265**, 6002-6008 (1990).
- 714 42 Butchbach, M. E., Tian, G., Guo, H. & Lin, C. L. Association of excitatory
715 amino acid transporters, especially EAAT2, with cholesterol-rich lipid raft
716 microdomains: importance for excitatory amino acid transporter
717 localization and function. *J Biol Chem* **279**, 34388-34396,
718 doi:10.1074/jbc.M403938200 (2004).
- 719 43 McIlwain, B. C., Vandenberg, R. J. & Ryan, R. M. Transport rates of a
720 glutamate transporter homologue are influenced by the lipid bilayer. *J*
721 *Biol Chem* **290**, 9780-9788, doi:10.1074/jbc.M114.630590 (2015).
- 722 44 Fairman, W. A., Sonders, M. S., Murdoch, G. H. & Amara, S. G. Arachidonic
723 acid elicits a substrate-gated proton current associated with the
724 glutamate transporter EAAT4. *Nat Neurosci* **1**, 105-113, doi:10.1038/355
725 (1998).
- 726 45 Raunser, S. *et al.* Heterologously expressed GLT-1 associates in
727 approximately 200-nm protein-lipid islands. *Biophys J* **91**, 3718-3726,
728 doi:10.1529/biophysj.106.086900 (2006).
- 729 46 Wales, T. E. & Engen, J. R. Hydrogen exchange mass spectrometry for the
730 analysis of protein dynamics. *Mass Spectrom Rev* **25**, 158-170,
731 doi:10.1002/mas.20064 (2006).

732 47 Konermann, L., Pan, J. & Liu, Y. H. Hydrogen exchange mass spectrometry
733 for studying protein structure and dynamics. *Chem Soc Rev* **40**, 1224-
734 1234, doi:10.1039/c0cs00113a (2011).

735 48 Shimamoto, K. *et al.* Characterization of novel L-threo-beta-
736 benzyloxyaspartate derivatives, potent blockers of the glutamate
737 transporters. *Mol Pharmacol* **65**, 1008-1015, doi:10.1124/mol.65.4.1008
738 (2004).

739 49 Watzke, N. & Grewer, C. The anion conductance of the glutamate
740 transporter EAAC1 depends on the direction of glutamate transport. *FEBS*
741 *Lett* **503**, 121-125 (2001).

742 50 Reyes, N., Oh, S. & Boudker, O. Binding thermodynamics of a glutamate
743 transporter homolog. *Nat Struct Mol Biol* **20**, 634-640,
744 doi:10.1038/nsmb.2548 (2013).

745 51 Kawate, T. & Gouaux, E. Fluorescence-detection size-exclusion
746 chromatography for precrystallization screening of integral membrane
747 proteins. *Structure* **14**, 673-681, doi:10.1016/j.str.2006.01.013 (2006).

748 52 Kabsch, W. Xds. *Acta Crystallogr D Biol Crystallogr* **66**, 125-132,
749 doi:10.1107/S0907444909047337 (2010).

750 53 Evans, P. R. & Murshudov, G. N. How good are my data and what is the
751 resolution? *Acta Crystallogr D Biol Crystallogr* **69**, 1204-1214,
752 doi:10.1107/S0907444913000061 (2013).

753 54 McCoy, A. J. *et al.* Phaser crystallographic software. *J Appl Crystallogr* **40**,
754 658-674, doi:10.1107/S0021889807021206 (2007).

755 55 Emsley, P., Lohkamp, B., Scott, W. G. & Cowtan, K. Features and
756 development of Coot. *Acta Crystallogr D Biol Crystallogr* **66**, 486-501,
757 doi:10.1107/S0907444910007493 (2010).

758 56 Blanc, E. *et al.* Refinement of severely incomplete structures with
759 maximum likelihood in BUSTER-TNT. *Acta Crystallogr D Biol Crystallogr*
760 **60**, 2210-2221, doi:10.1107/S0907444904016427 (2004).

761 57 O'Brien, D. P. *et al.* Structural models of intrinsically disordered and
762 calcium-bound folded states of a protein adapted for secretion. *Sci Rep* **5**,
763 14223, doi:10.1038/srep14223 (2015).

764 58 Hourdel, V. *et al.* MEMHDX: An interactive tool to expedite the statistical
765 validation and visualization of large HDX-MS datasets. *Bioinformatics*,
766 doi:10.1093/bioinformatics/btw420 (2016).

767 59 Waterhouse, A. M., Procter, J. B., Martin, D. M., Clamp, M. & Barton, G. J.
768 Jalview Version 2--a multiple sequence alignment editor and analysis
769 workbench. *Bioinformatics* **25**, 1189-1191,
770 doi:10.1093/bioinformatics/btp033 (2009).

771

772

773

774 **Acknowledgements** We thank Olga Boudker for comments on the manuscript and
775 discussion on consensus mutagenesis; Petya V. Krasteva for comments on the
776 manuscript; Ahmed Haouz and the staff at the crystallogenes core facility of the
777 Institut Pasteur for assistance with crystallization screens; Staff at Synchrotron Soleil
778 and the European Synchrotron Radiation Facility for beam time allocation and
779 assistance with data collection; Darragh O'Brien for discussion of HDX results. The
780 work was funded by the ERC Starting grant 309657 (N.R.). Further support from G5
781 Institut Pasteur funds (N.R.), CACSICE grant (ANR-11-EQPX-008), and CNRS
782 UMR3528 (N.R, J.C.-R.) is acknowledged.

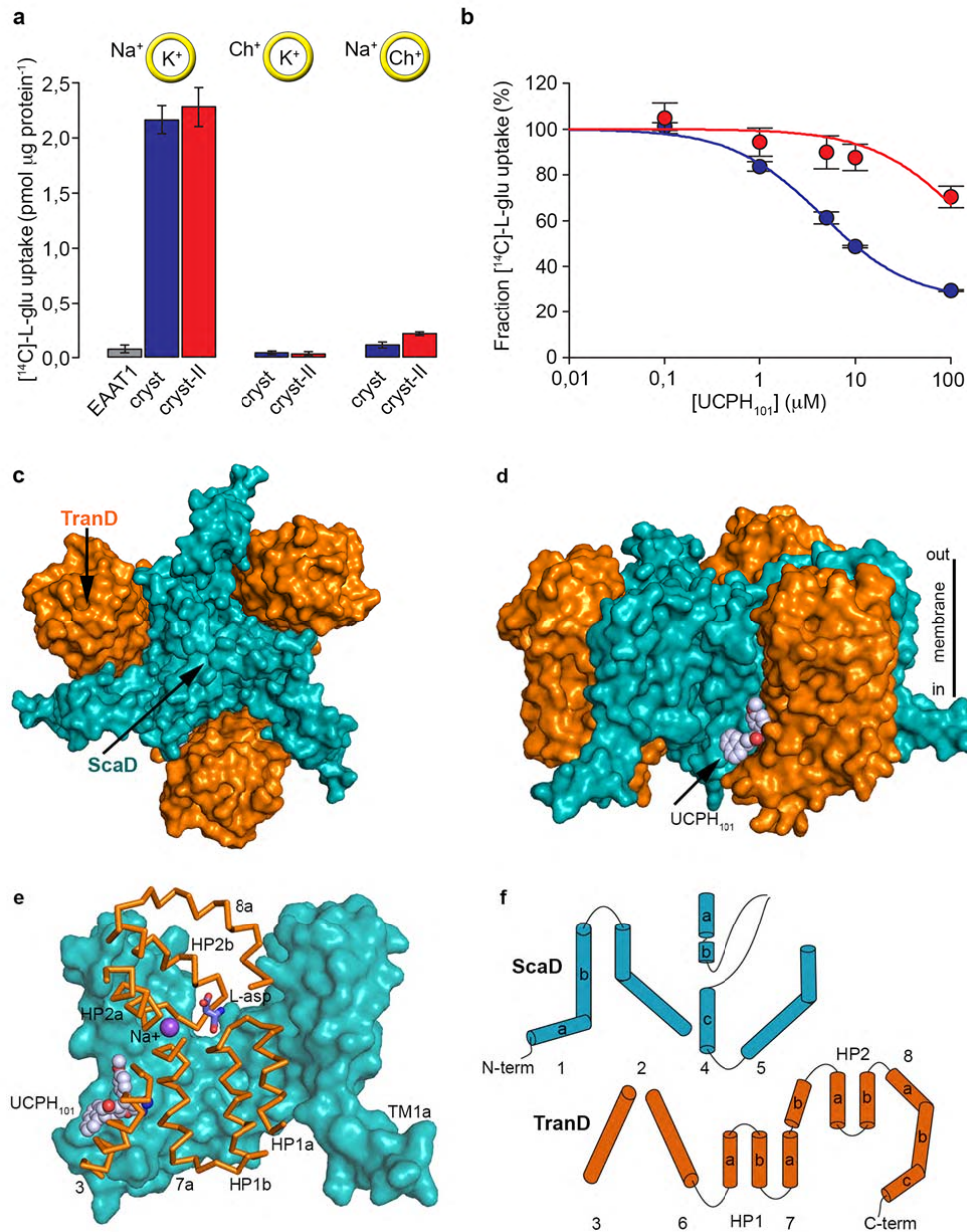
783

784 **Author contribution**

785 J.C.C.-T., and R.A. optimized and performed protein expression, purification and
786 crystallization, and R.A. performed molecular biology; J.C.C.-T., R.A., and N.R.
787 collected crystallographic data, and J.C.C.-T., P.L., and N.R. analyzed diffraction data
788 and structures; E.C. and R.A performed and analyzed uptake experiments; E.C.
789 prepared protein samples for HDX-MS; S.B. collected and analyzed HDX-MS data
790 with help from E.C.; All authors contributed to the experimental design of the project
791 and manuscript preparation. N.R. conceived and supervised the project.

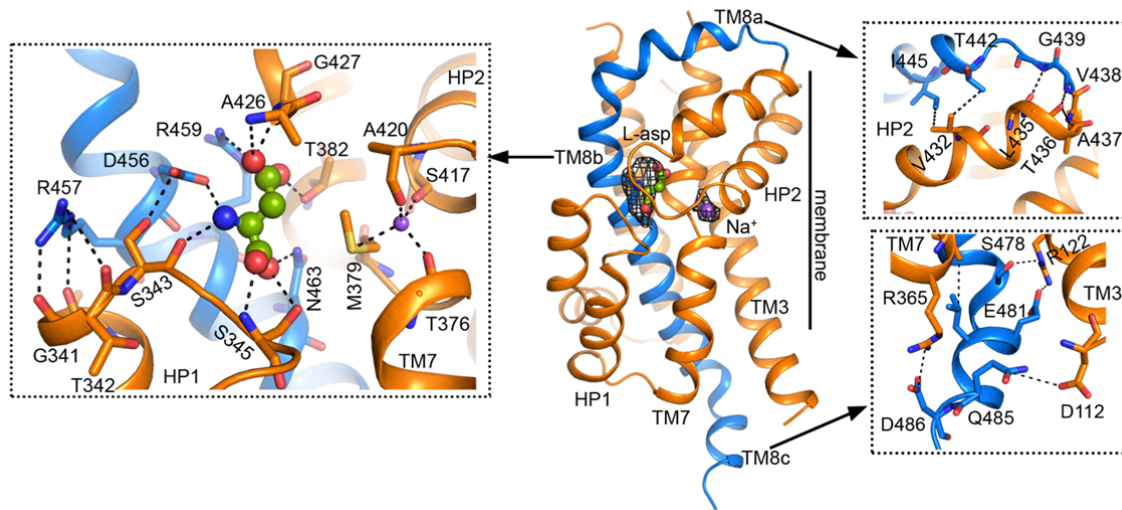
792

793 **Author Information** Coordinates and structure factors for EAAT1_{cryst}-UCPH₁₀₁,
794 EAAT1_{cryst}-UCPH₁₀₁-TBOA_{TFB}, EAAT1_{cryst-II}-UCPH₁₀₁, and EAAT1_{cryst-II} crystal
795 structures have been deposited in the Protein Data Bank with accession codes 5LLM,
796 5MJU, 5LM4, 5LLU, respectively. The authors declare no competing financial
797 interests. Correspondence and requests for materials should be addressed to N.R.
798 (nreyes@pasteur.fr)



802 **Figure 1 | Function and architecture of EAAT1_{cryst}.** **a-b**, Uptake of radioactive L-
803 glutamate by purified EAAT1 (grey), EAAT1_{cryst} (blue), and EAAT1_{cryst-II} (red)
804 reconstituted in liposomes. Transport was abolished when choline (Ch⁺) was used as
805 the main cation in the extra- or intra-liposomal solutions (yellow circles) (**a**).
806 UCPH₁₀₁ inhibits glutamate transport in a concentration dependent manner (**b**). Plots
807 depict an average of three independent experiments performed with duplicate
808 measurements, and error bars represent s.e.m. **c-d**, Structure of EAAT1_{cryst} trimer
809 viewed from the extracellular solution (**c**) and from the membrane (**d**), with the ScaD
810 (teal) and TranD (orange) as surfaces, and UCPH₁₀₁ bound between them (white
811 spheres). **e**, EAAT1_{cryst} monomer viewed parallel to the membrane. The ScaD domain
812 is represented as surface (teal), and several helices and loops in the TranD (orange)
813 have been removed for clarity of display. **f**, Domain organization diagram of
814 EAAT1_{cryst} monomer.

815
816
817
818
819



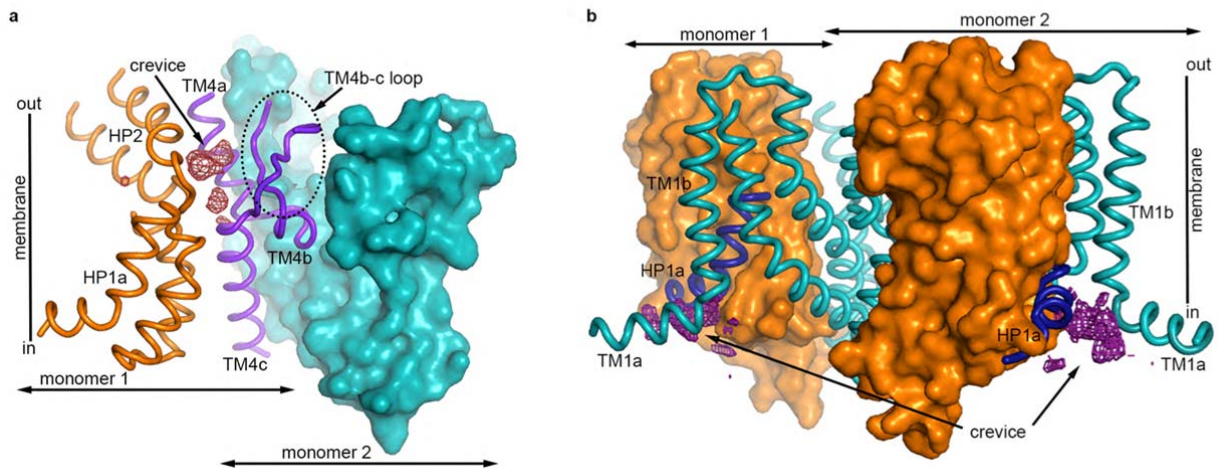
820
821

822 **Figure 2 | Transport domain.** EAAT1_{cryt} transport domain viewed from the
823 membrane with substrate (spheres) and one sodium ion (purple spheres) bound. Omit
824 Fo-Fc densities contoured at 2.3 σ (black mesh) show the position of the ligands.
825 TM8a-c (blue) interacts with other regions on the TranD (orange), including HP1 (left
826 inset), HP2 (upper right inset), and TM3 and TM7 (lower right inset).

827

828

829



830

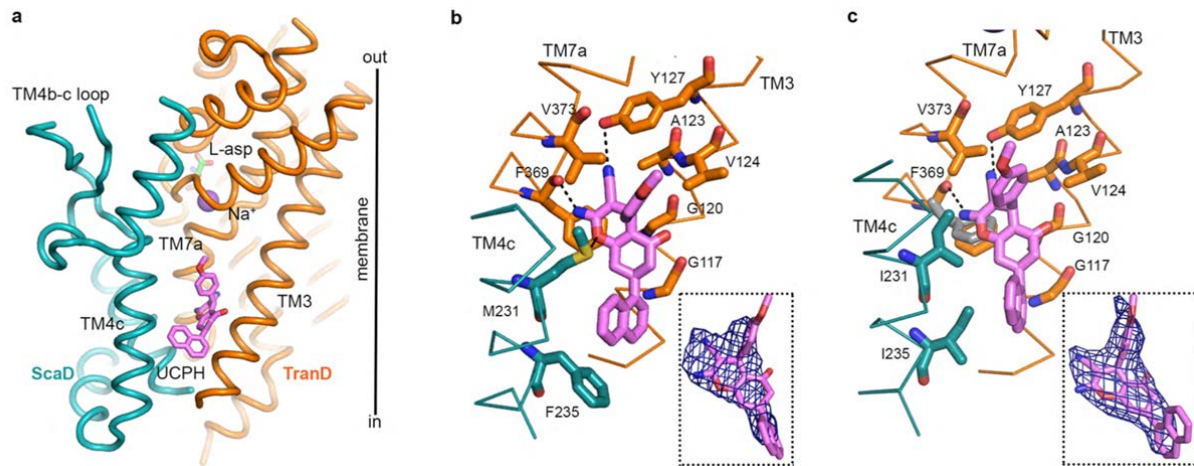
831

832 **Figure 3 | Scaffold domain.** **a**, TM4 (purple) makes extensive contacts with the ScaD
833 of the neighboring monomer (monomer 2, teal surface), and the TranD (orange) of its
834 own polypeptide (monomer 1). The TranD of monomer 2, and several TMs of
835 monomer 1 were removed for clarity of display. Fo-Fc density in the HP2-TM4
836 crevice is contoured at 2.7σ (red mesh). **b**, Two monomers of EAAT_{cryst} show TM1a
837 laying parallel to the membrane. The third monomer is not shown. TM1 (teal) and
838 HP1a (dark blue) form a hydrophobic crevice containing non-protein Fo-Fc density
839 (purple mesh, contour 2.7σ).

840

841

842



843

844

845 **Figure 4 | UCPH₁₀₁ binding site.** **a**, Lateral view of EAAT1_{cryst} monomer from the

846 membrane showing UCPH₁₀₁ bound (pink) between the TranD (orange) and ScaD

847 (teal). **b-c**, UCPH₁₀₁ (pink) coordination and Fo-Fc densities contoured at 2.0 σ (blue

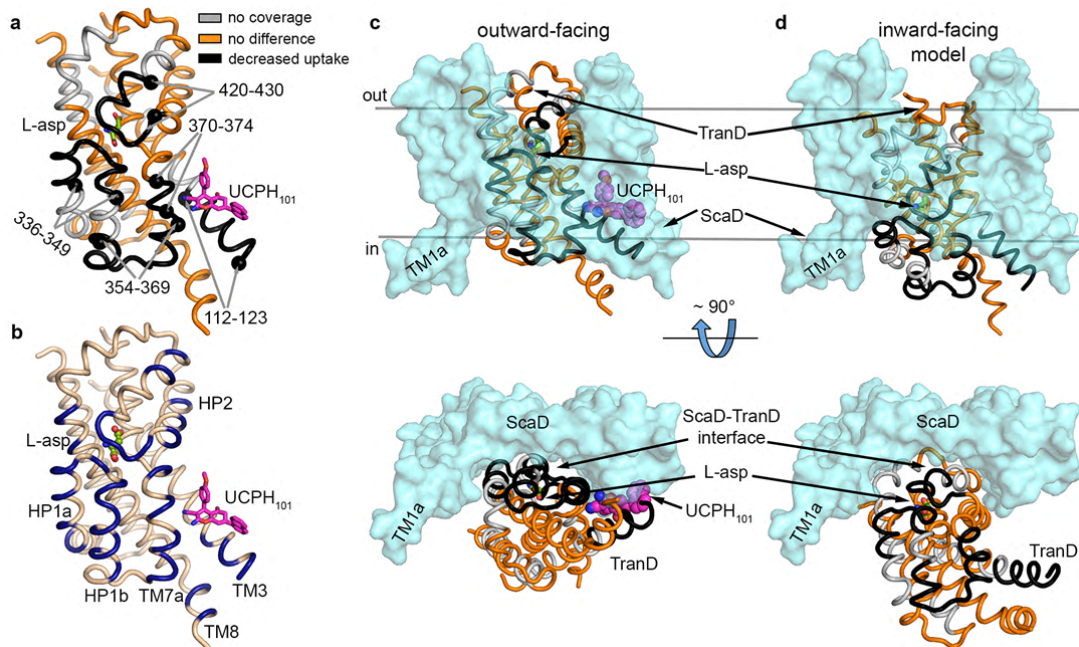
848 mesh) in EAAT1_{cryst} (**b**) and EAAT1_{cryst-II} (**c**), respectively. Side chains of residues in

849 TM3, TM4c, and TM7 involved in coordination are shown. F369 side chain moves

850 outward in the EAAT1_{cryst-II} unbound state (grey) (**c**).

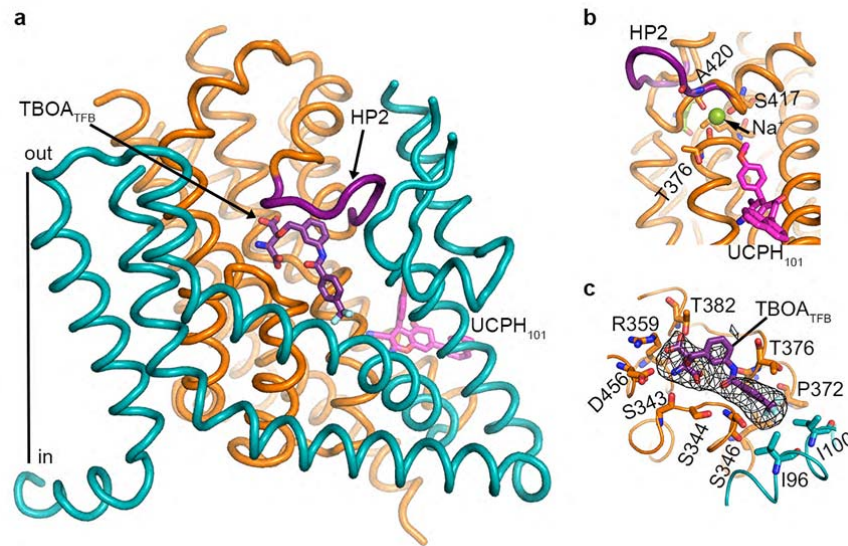
851

852
853
854
855



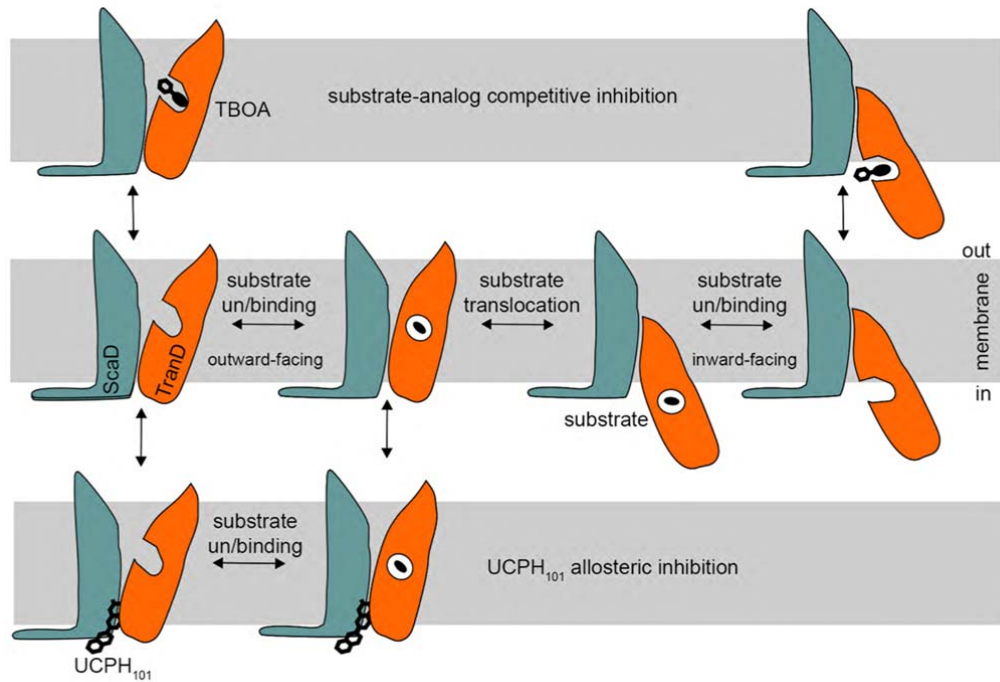
856
857 **Figure 5 | Transport domain dynamics.** **a**, UCPH₁₀₁ decreased deuterium uptake in
858 several regions (black) of the TranD at the interface with the ScaD. The alpha carbon
859 atoms of the limiting residues for these regions are shown as back spheres.
860 Unaffected regions of the TranD (orange) or those not detected during HDX-MS
861 analysis (grey) are also shown (sequence coverage ~77%). **b**, Residues of the
862 EAAT1_{cryc} TranD buried at the interface with the ScaD, in the UPCH₁₀₁-bound
863 outward-facing state, are colored dark blue for comparison with **(a)**. **c-d**, Comparison
864 of EAAT1_{cryc} structure in the UPCH₁₀₁-bound outward-facing state **(c)** with a model
865 of an inward-facing state based on the GltPh “unlocked” state (PDB 4X2S) **(d)**. The
866 ScaD domain (pseudo-transparent surface cyan) is in identical positions in the
867 structure and the model, while the TranD (color code as in **a**) undergoes a large rigid
868 body movement towards the cytoplasm.
869

870
871
872
873
874
875
876
877
878
879
880



881 **Figure 6 | UCPH₁₀₁-TBOA_{TFB} bound EAAT1_{cryst} structure.** **a**, The TranD and
882 ScaD of the EAAT1_{cryst} monomer are represented in orange and cyan, respectively.
883 The movement of HP2 (purple) partly exposes the substrate-binding pocket to the
884 solvent and shows a molecule of TBOA_{TFB} (purple sticks) bound to it. UCPH₁₀₁ is
885 also observed in this structure (pink sticks). **b**, The tip of HP2 moves as much as 9.5
886 Å in the UCPH₁₀₁-TBOA_{TFB}- (purple), compared to the UCPH₁₀₁-substrate bound
887 (orange) structures, moving the carbonyl oxygen of A420 away from Na₂ (green
888 sphere). **c**, Omit map Fo-Fc density for the TBOA_{TFB} molecule is contoured at 2.3σ
889 (black mesh), and some of the residues at Van der Waals or H-bond distance from
890 the compound are represented as sticks.

891
892
893
894
895
896
897



898
899
900
901
902
903
904
905
906
907

Figure 7 | EAAT1 inhibitory mechanisms. Schematic representation of the molecular mechanisms of action of TBOA-like competitive and UCPH₁₀₁-like allosteric inhibitors in EAAT1. Competitive inhibitors, bind to the substrate-binding pocket in the TranD and preclude substrate (black ellipse) binding from both sides of the membrane. UCPH₁₀₁-like compounds bind at the TranD-ScaD interface and block the movement of the TranD (orange) relative to the ScaD (teal), but allow substrate binding from the extracellular solution.

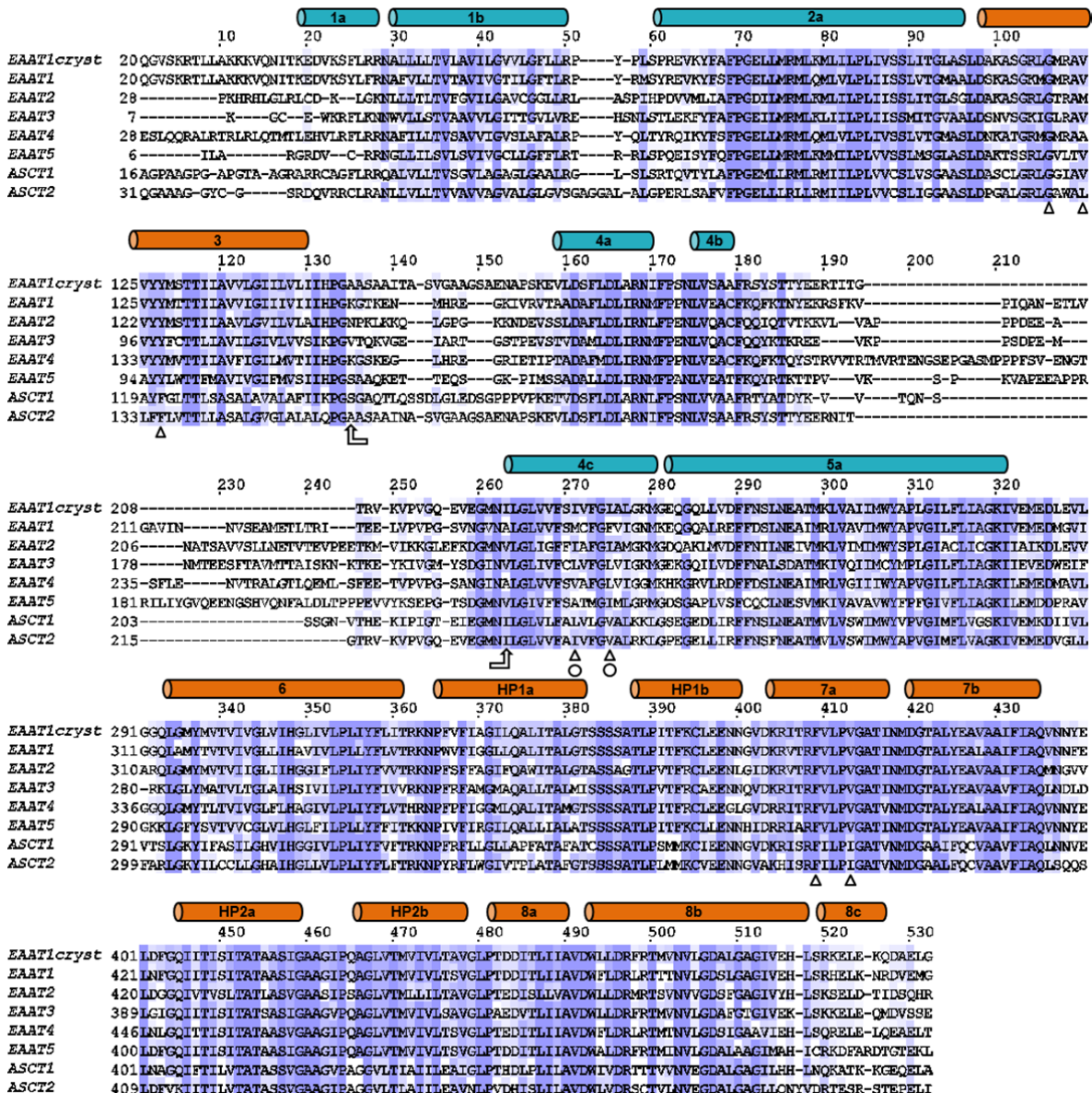
908
909

Extended Data Table 1. Data collection and refinement statistics.

	EAAT1 _{cryst} UCPH ₁₀₁ bound	EAAT1 _{cryst-II} UCPH ₁₀₁ bound	EAAT1 _{cryst-II}	EAAT1 _{cryst} UCPH ₁₀₁ and TBOA _{TFB} bound
Data collection*				
Space group	<i>P</i> 6 ₃	<i>P</i> 6 ₃	<i>P</i> 6 ₃	<i>P</i> 6 ₃
Cell dimensions				
<i>a=b, c</i> (Å)	123.27, 89.87	123.11, 89.62	123.32, 89.57	124.33, 90.81
$\alpha=\beta, \gamma$ (°)	90.0, 120.0	90.0, 120.0	90.0, 120.0	90.0, 120.0
Wavelength	0.979	0.976	1.009	0.977
Resolution (Å)	45.89- 3.25 (3.34-3.25)	45.82- 3.1 (3.18-3.1)	45.87- 3.32 (3.41-3.32)	46.31- 3.71 (3.81-3.71)
Anisotropy direction [§]				
Resolution where $CC_{1/2} > 0.3$				
Overall (Å)	3.37	3.1	3.32	3.71
along h, k axis (Å)	3.75	3.68	3.85	4.35
along l axis (Å)	3.25	3.1	3.32	3.71
Measured reflections	333978 (24261)	290672 (21906)	326273 (21829)	141904 (11176)
Unique reflections	12338 (902)	14115 (1 032)	11556 (834)	8570 (628)
Completeness (%)	100 (100)	99.9 (99.9)	100 (100)	99.9 (100.0)
Mn (I) half-set correlation	0.99 (0.22)	1 (0.43)	0.99 (0.31)	0.99 (0.373)
<i>I</i> / σ (<i>I</i>)	11.7 (0.7)	15.8 (0.8)	13 (0.7)	12.1 (0.9)
<i>R</i> _{merge}	0.20 (6.90)	0.1 (6.71)	0.15 (8.16)	0.14 (3.71)
Redundancy	27.1 (26.9)	20.6 (21.2)	28.2 (26.2)	16.3 (14.3)
Structure determination				
Refinement				
Resolution cut-off (Å)	45.89- 3.25	45.80- 3.10	20.00- 3.32	25.00- 3.71
No. of Work / Test reflections	9891/475	10725/528	9251/445	6860/684
<i>R</i> _{cryst} (%) / <i>R</i> _{free} (%)	21.9/24.1	21.7/25.9	20.9/25.3	22.7/25.4
No. of protein atoms	3002	2960	2995	3008
No. of heteroatoms	42	42	10	62
<i>B</i> factors (Å) ²				
Protein	129.5	111.8	137.0	135.5
Heteroatoms	107.3	99.5	125.6	132.7
R.m.s. deviations from ideal				
Bond lengths (Å)	0.009	0.01	0.009	0.009
Bond angles (°)	1.06	1.12	1.05	1.03

910
911
912
913
914

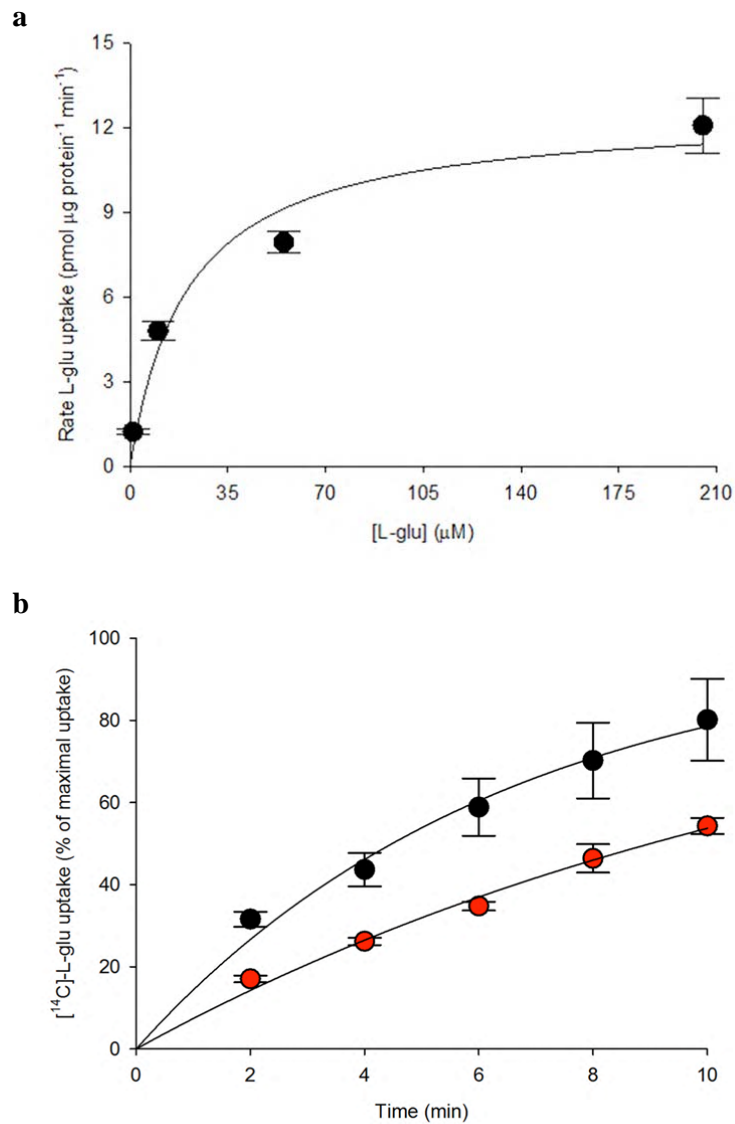
One crystal was used to collect diffraction datasets for each structure, except in the EAAT1_{cryst} UCPH₁₀₁ and TFB-TBOA bound structure, where datasets from three crystals were merged. 5% of reflections were used for calculation of *R*_{free}.
*Values in parentheses are for the highest-resolution shell.
§The anisotropy directions where computed with AIMLESS.



915

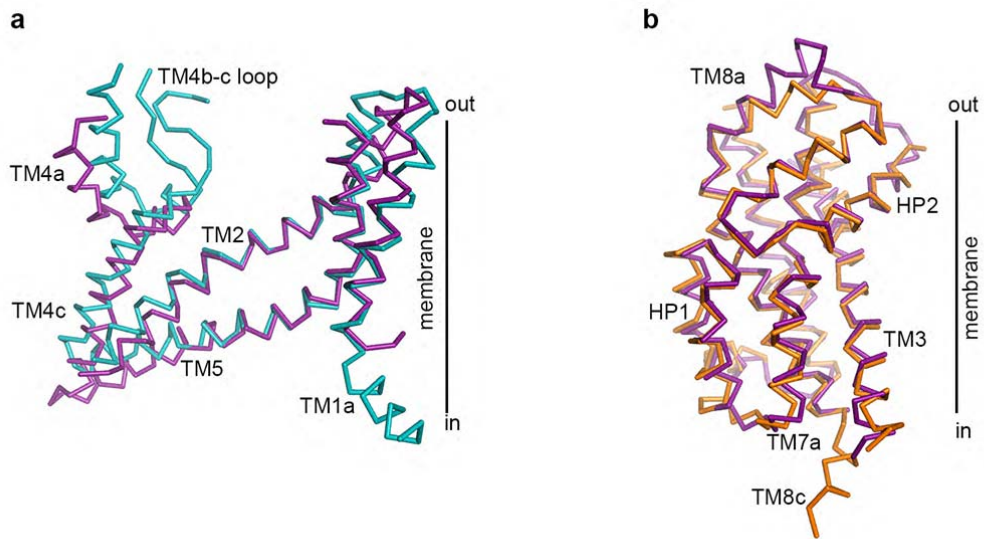
916 **Extended Data Figure 1 | Alignment of human SLC1 transporters.** Amino acid
917 sequences of EAAT1-5, ASCT1-2 and EAAT1_{crist} are compared. The boundaries of the
918 α -helices (cylinders) in the TranD (orange) and the ScaD (teal) seen in the
919 EAAT1_{crist} structure are shown. In order to confer crystallizability, the region
920 between TM3 and TM4c (arrows) from ASCT2 was transferred to a thermally
921 stabilized EAAT1. To further improve crystal formation in the absence of UPCH₁₀₁,
922 mutations M231I and F235I (circles) were introduced to generate EAAT1_{crist-II}. These
923 substitutions are found in EAAT2. Other residues involved in UPCH₁₀₁ coordination
924 are more conserved (triangles). Sequences were aligned with Jalview⁵⁹.

925
926
927
928
929
930
931
932
933
934
935
936
937
938
939
940



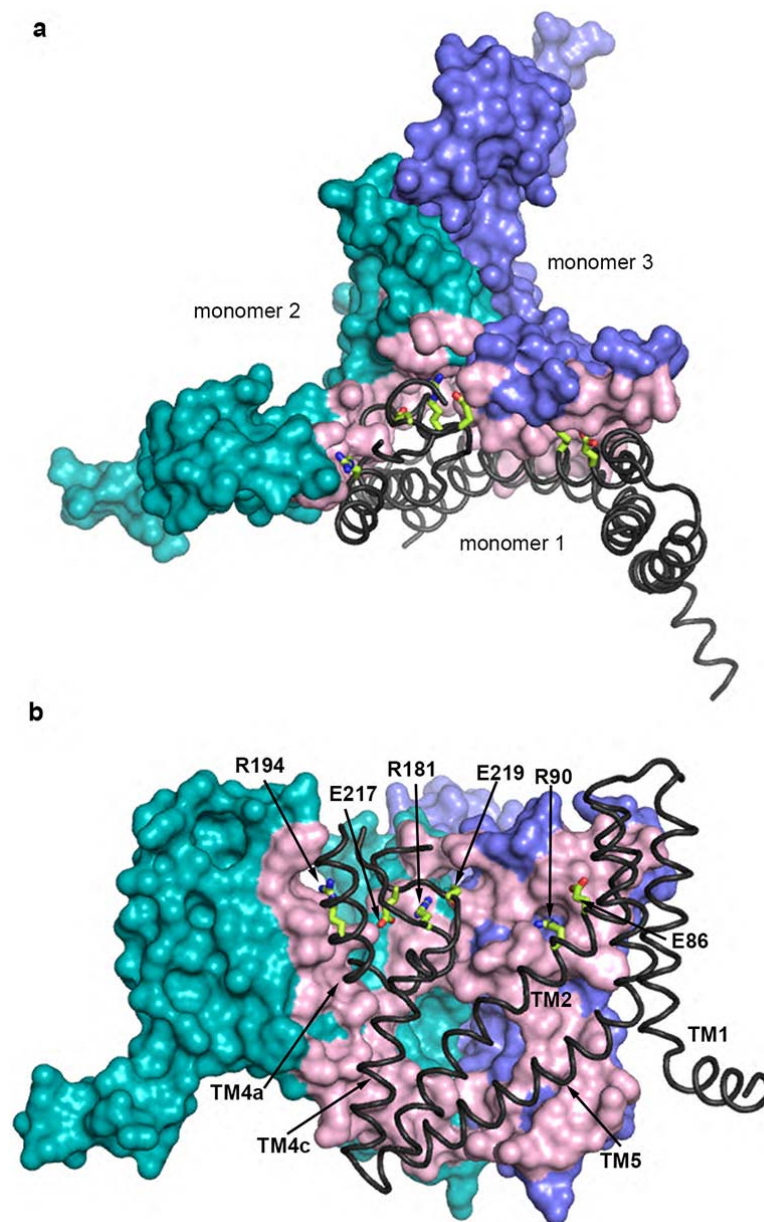
Extended Data Figure 2 | EAAT1_{cryst} and EAAT1 glutamate uptake. **a**, Initial rates of L-glutamate uptake from purified EAAT1_{cryst} reconstituted in liposomes. The solid line is the fit of a Michaelis-Menten equation to the data with $K_M=21 \pm 10 \mu\text{M}$ and $V_{\text{max}}= 13 \pm 1 \text{ pmol } \mu\text{g}^{-1} \text{ protein min}^{-1}$. The graph is the mean of three independent experiments, and error bars represent s.e.m.. **b**, L-glutamate uptake was measured in HEK293 cells expressing WT EAAT1 (black circles) and a truncated mutant beyond E501 (red symbols). The initial rate of uptake decreased by ~ 2 -fold in the EAAT1 truncated mutant. Data were normalized to the asymptotic level of glutamate uptake based on a monoexponential function. The rates obtained from the fits were 0.16 ± 0.03 and $0.08 \pm 0.03 \text{ min}^{-1}$ for EAAT1 and the truncated mutant, respectively. The graphs are means of 4 independent experiments done in duplicates. Error bars represent the s.e.m..

941
942
943
944



945
946
947
948
949
950

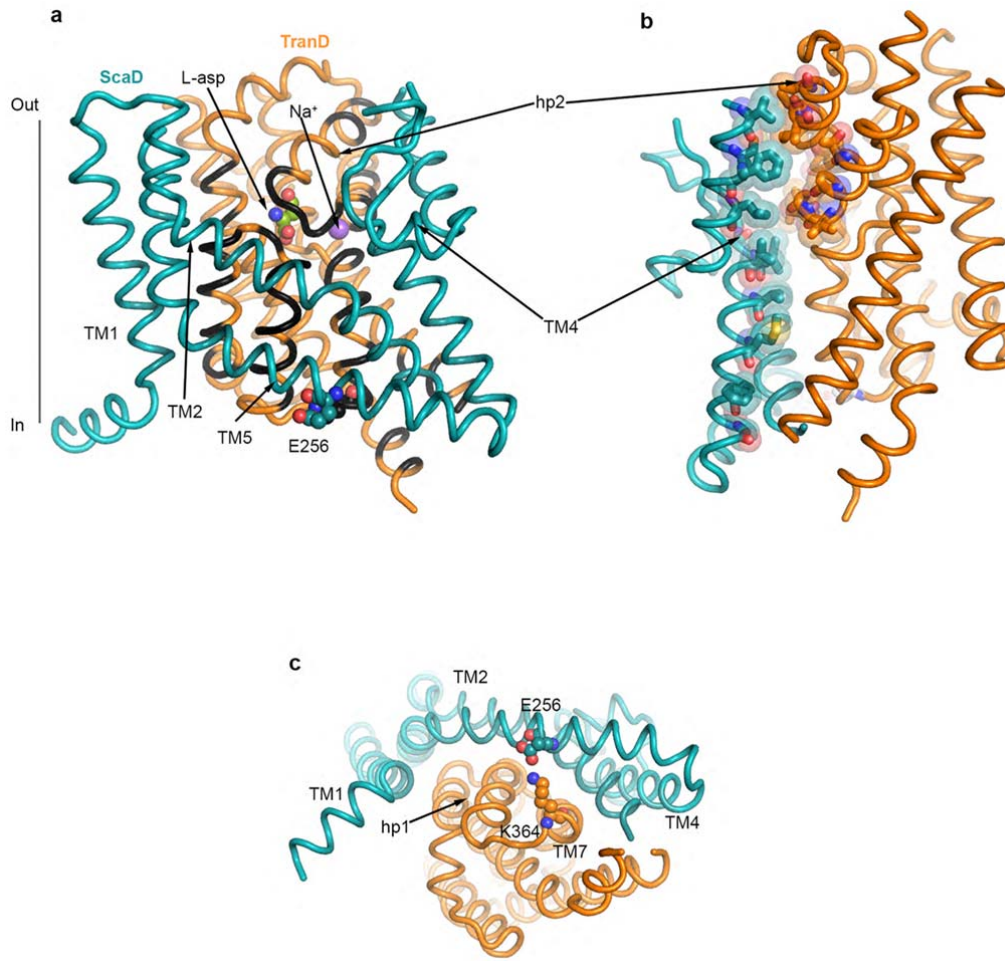
Extended Data Figure 3 | EAAT1_{cryst} and GltPh structural comparison. a-b
EAAT1_{cryst} aligns to a monomer of GltPh (PDB 2NWL) with α -carbon r.m.s.d. of 1.4 Å. The ScaDs (EAAT1_{cryst} teal, and GltPh purple, a), and TranDs (EAAT1_{cryst} orange and GltPh, purple, b) are shown separately for clarity of display.



951
 952
 953
 954
 955
 956
 957
 958
 959
 960
 961
 962
 963
 964
 965

Extended Data Figure 4 | EAAT1_{cryst} trimeric interface. **a-b**, Interface of three ScaDs of the EAAT1_{cryst} UCPH₁₀₁-bound structure viewed from the extracellular side (**a**) and from the membrane (**b**). The TranDs are not shown. The ScaD of one monomer (black) makes extensive contacts with the two other subunits (teal and purple surfaces). The surface area in monomers 2 and 3 buried by monomer 1, is colored in light pink. Only residues that contribute $\geq 10 \text{ \AA}^2$ of buried surface area are highlighted. Side chains of residues that form intermolecular salt bridges are colored in green (sticks).

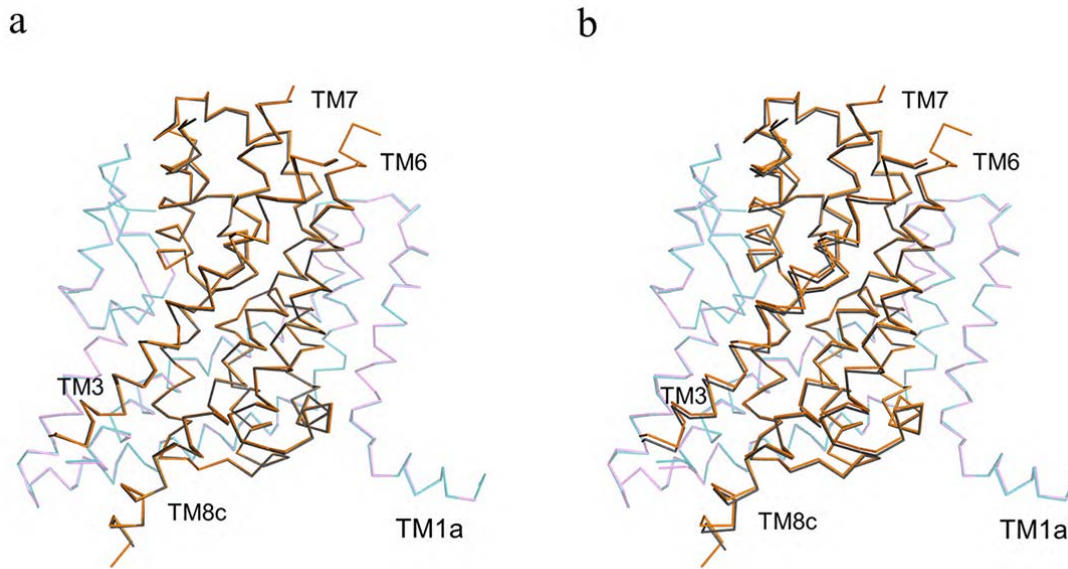
966
967
968
969
970



971
972
973
974
975
976
977
978
979
980
981

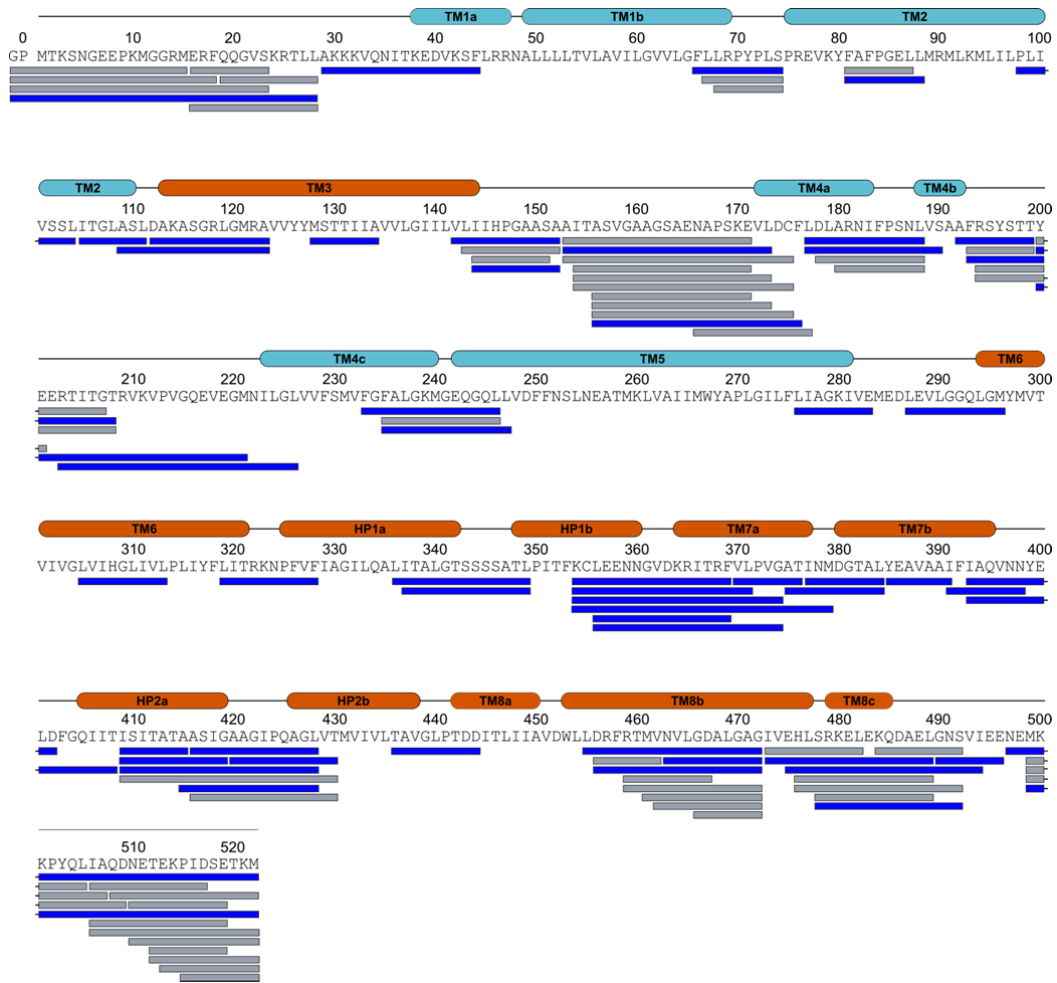
Extended Data Figure 5 | TranD-ScaD interface. **a-b**, EAAT1_{cryst} monomer viewed from the membrane (solid black line). Residues in the TranD (colored black) bury 1,760 Å² at the interface with the ScaD (**a**). This interface extends to the extracellular side of the transporter through interactions between HP2-TM4 (sticks and pseudo-transparent spheres) (**b**). **c**, Cytoplasmic view of the monomer displaying the salt bridge between TM7 and TM5.

982
983
984
985
986
987
988
989
990
991



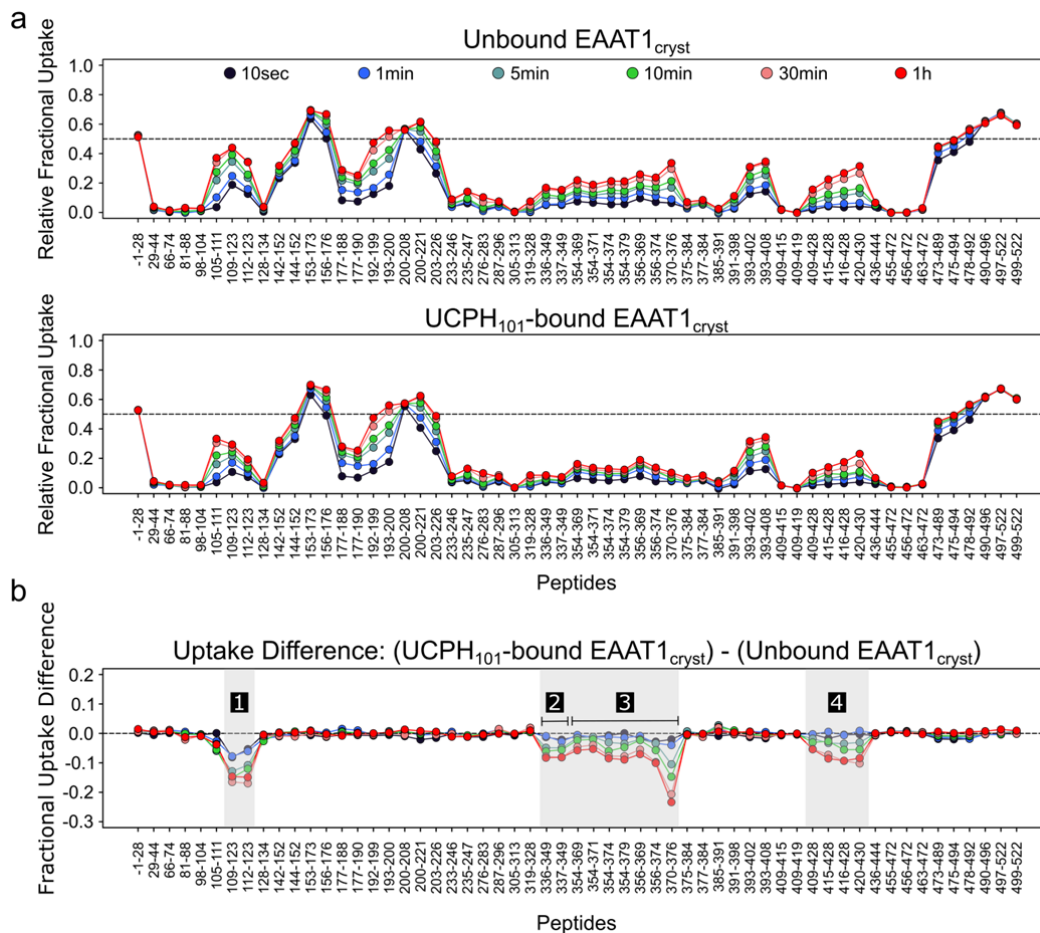
992
993
994
995
996
997
998
999
1000
1001
1002
1003
1004
1005

Extended Data Figure 6 | Superposition of EAAT1_{cryst} and EAAT1_{cryst-II} structures. a-b, The transport domains of EAAT1_{cryst} (teal) and EAAT1_{cryst-II} (pink) UCPH₁₀₁-bound structures superimpose accurately after aligning their scaffold domains (a). The overall α -carbon r.m.s.d. was 0.3 Å. However, the same alignment done with EAAT1_{cryst-II} UCPH₁₀₁-bound and -unbound structures shows a small but global movement of the transport domain (b), with a small increase in the overall α -carbon r.m.s.d. of 0.1 Å.



1006
 1007
 1008
 1009
 1010
 1011
 1012
 1013
 1014
 1015
 1016
 1017
 1018

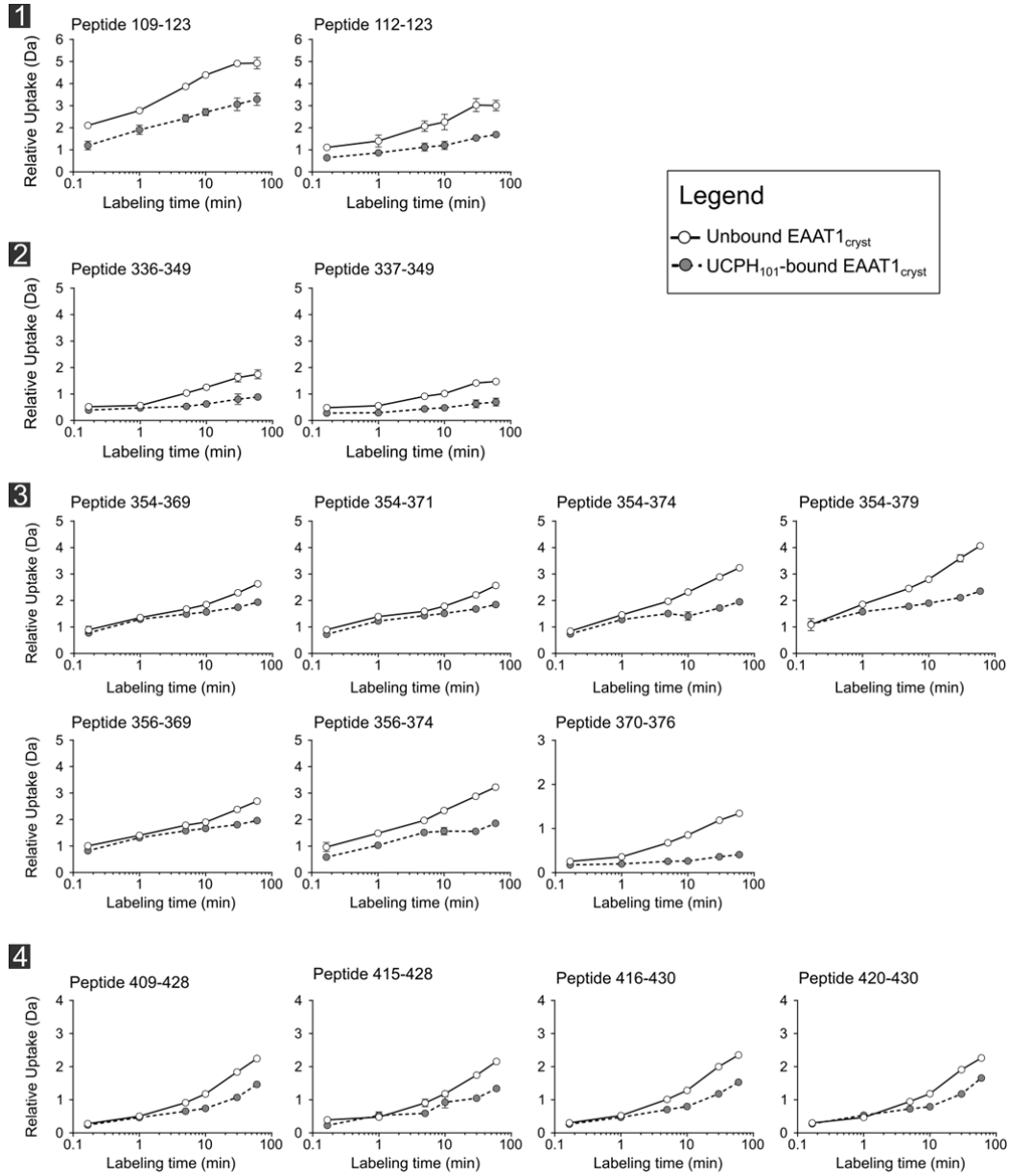
Extended Data Figure 7 | Peptide coverage map of EAAT1_{crist}. A total of 111 peptides covering 76.3% of the EAAT1_{crist} sequence were identified by data independent MS/MS acquisition after 2 min digestion with immobilized pepsin. Each bar below the EAAT1_{crist} sequence corresponds to a unique peptide. The 57 peptides colored in blue were further selected for HDX-MS data extraction and analysis. The two additional N-terminal residues (*i.e.*, GP) that remain after protein purification are also shown. The transmembrane helices (TM) of the TranD (orange) and the ScaD (cyan) are indicated above the sequence.



1019
 1020
 1021
 1022
 1023
 1024
 1025
 1026
 1027
 1028
 1029
 1030
 1031
 1032
 1033

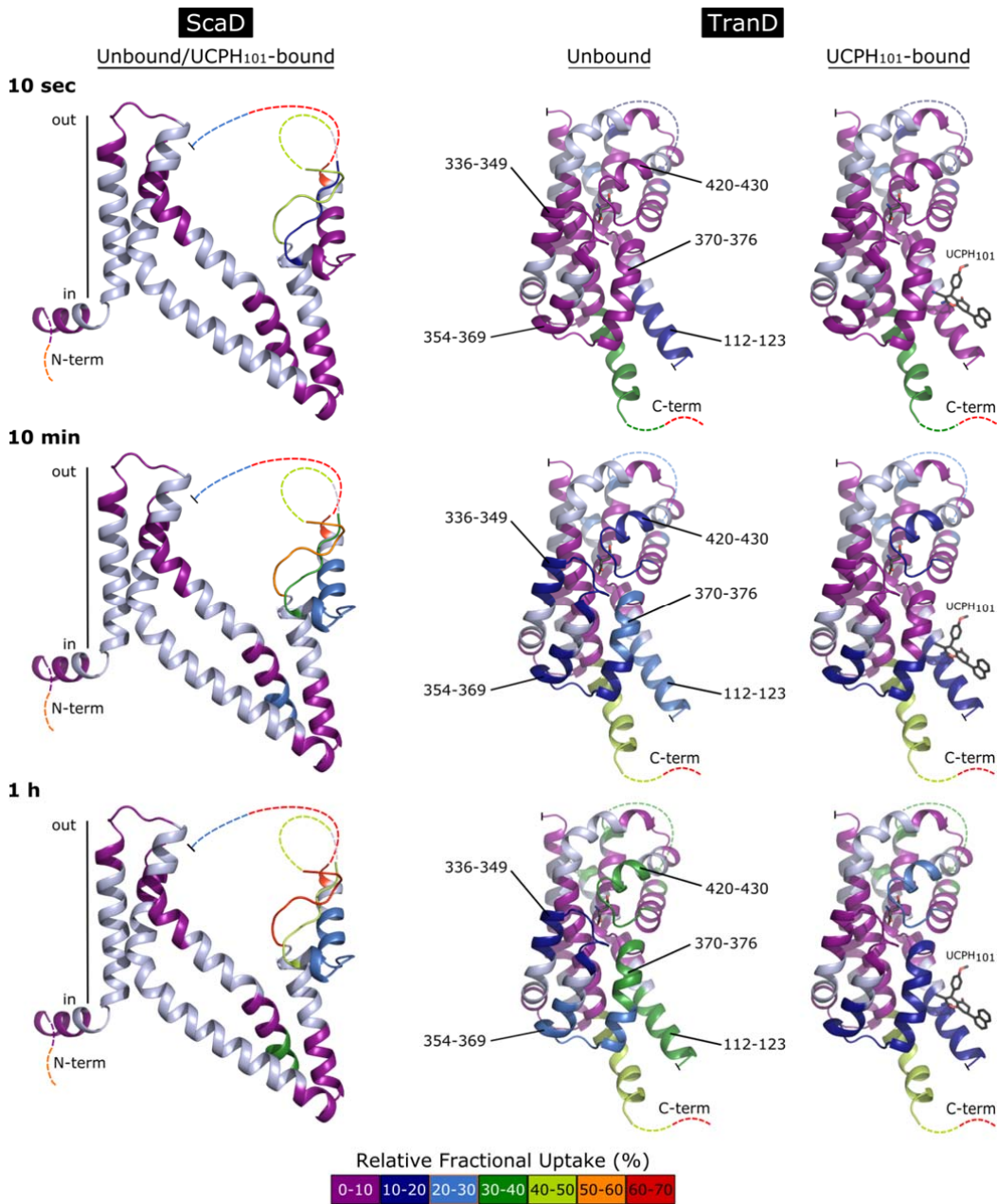
Extended Data Figure 8 | UCPH₁₀₁ effect on the local hydrogen exchange behavior of EAAT1_{cryst}. **a**, HDX profiles of EAAT1_{cryst} (see Methods) in the apo (upper panel) and UCPH₁₀₁-bound state (middle panel). The relative fractional uptake determined for each peptide and at each time point is plotted as a function of peptide position. The black to red lines correspond to data acquired from 10 sec up to 1h, respectively. **b**, The fractional uptake difference plot was generated by subtracting the deuterium uptake values in the UCPH₁₀₁-unbound from those in the bound state. Negative uptake difference indicates UCPH₁₀₁-induced decrease in amide hydrogen exchange. Each dot corresponds to an average of three independent HDX-MS experiments. The four regions (labeled 1 to 4) showing a statistically significant modification ($p < 0.01$) of deuterium uptake upon binding of UCPH₁₀₁ are highlighted in grey.

1034



1035
1036
1037
1038
1039
1040
1041
1042
1043

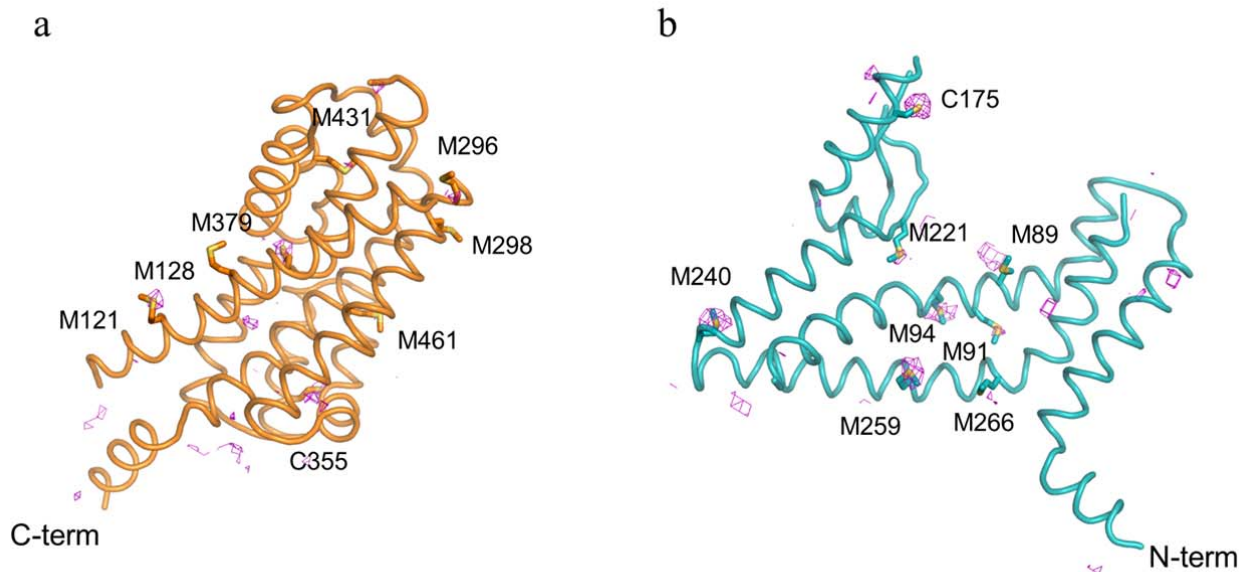
Extended Data Figure 9 | Deuterium uptake curves for the peptides covering the regions of EAAT1_{cryst} affected by UCPH₁₀₁. Each symbol corresponds to the average value of three independent replicates in the absence (open circles) and presence of UCPH₁₀₁ (grey circles). Error bars represent S.D. and are only displayed for values > 0.15 Da.



1044
 1045
 1046
 1047
 1048
 1049
 1050
 1051
 1052
 1053
 1054
 1055

Extended Data Figure 10 | HDX-MS results mapped on the crystal structure of ScaD and TranD of EAAT1_{cryst} in the unbound and UCPH₁₀₁-bound state. The color code at the bottom shows the average relative fractional uptake measured in both domains after 10 sec (upper panel), 10 min (middle panel) and 1h (lower panel) labeling. Missing regions in the crystal structure are represented by dashed lines. Peptides showing a statistically significant ($p < 0.01$) modification of deuterium uptake upon UCPH₁₀₁ binding are labeled. Uncovered regions are colored in light blue.

1056
1057
1058
1059
1060
1061
1062
1063



1064
1065
1066
1067
1068
1069
1070
1071
1072
1073
1074
1075
1076
1077

Extended Data Figure 11 | Sulfur anomalous difference Fourier maps. Anomalous difference Fourier maps contoured at the 2.8σ (pink mesh), from data collected at low energy X-rays (1.77 \AA), show the correct sequence registry in both the TranD (orange, **a**) and the ScaD (teal, **b**).